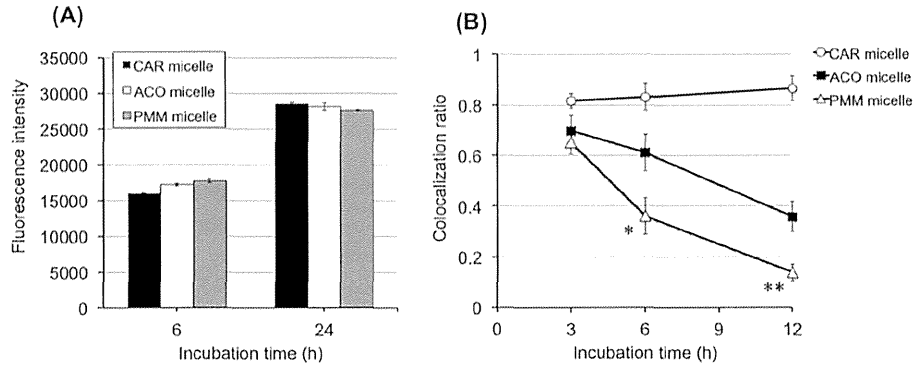

Figure 3. A) Cellular uptake efficiency of Cy5-siLuc delivered by hybrid micelles in SKOV3-Luc cells after 6 h incubation and 24 h incubation (100×10^{-9} M siRNA). Results are expressed as mean ± SEM ($n = 3$). (B) Time-dependent change in colocalization ratio of Alexa647-siLuc (red) with CellLight Late Endosomes-GFP (green) in SKOV3-Luc cells (200×10^{-9} M siRNA). The data are represented as mean ± SEM obtained from 14 cells ($^{*}p < 0.05$, $^{**}p < 0.01$).

and the micelles prepared with PEG–PAsp(DET–CAR) as a non-charge-conversion control polymer (nonCCP), in 6 h incubation. The uptake was further increased by prolonging the incubation time to 24 h. Importantly, almost the same cellular internalization profiles were observed among the three micelles, presumably because they have similar PEGylated shell structures. Next, the intracellular trafficking of hybrid micelles was investigated as a critical step following the cellular internalization. In particular, the colocalization of hybrid micelles (or the siRNA payload) with the late endosomes was focused to verify the endosome-escaping functionality of PEG–PAsp(DET–PMM) in comparison with PEG–PAsp(DET–ACO) and PEG–PAsp(DET–CAR). SKOV3-Luc cells were incubated with each hybrid micelle prepared with Alexa647-siLuc, and then, the transfection medium containing the hybrid micelles was exchanged with the fresh one without micelle samples, followed by additional incubation before confocal laser scanning microscope (CLSM) imaging. The intracellular Alexa647-siLuc was shown red and also the endosomal membrane was stained with CellLight Late Endosomes-GFP (green), thereby their colocalization points within the cells should be shown yellow in the merged CLSM images (Figure S7, Supporting Information). Then, the colocalization ratio of Alexa647-siLuc with the stained late endosomes at the designated time points was calculated by pixel counting for each hybrid micelle (Figure 3B), as described in Supporting Information. The CCP-integrated micelles, i.e., PMM and ACO micelles, showed time-dependent decreases in the colocalization ratio from 3 to 12 h, whereas the colocalization ratio of the nonCCP-integrated, CAR micelles was not significantly altered. This result strongly suggests the facilitated endosomal escape of Alexa647-siLuc by the CCPs integrated into the hybrid micelles. Further, the colocalization ratio of PMM micelles was significantly lower than that of ACO micelles, demonstrating stronger endosome-escaping functionality of the CCP integrated with PAsp(DET–PMM). On the contrary, the apparently high colocalization ratios of CAR micelles indicate that the hybrid micelles without CCPs could not effectively induce the endosome disruption under the tested condition. These results are consistent with the polymer design concept that more rapid conversion of CCPs to the endosome-disrupting polycation PAsp(DET) at an endosomal acidic pH of 5.5 should enable more efficient endosomal escape of hybrid micelles.

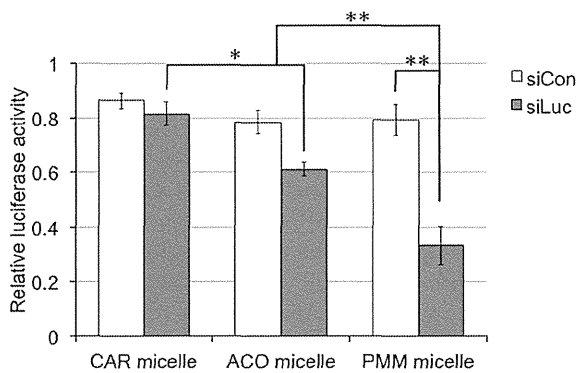

Figure 4. Luciferase gene silencing efficiency of CAR micelles, ACO micelles, and PMM micelles in SKOV3-Luc cells. The cells were incubated with each micelle incorporating siLuc (target sequence) or siCon (control sequence) at 50×10^{-9} M siRNA for 48 h, followed by a conventional luciferase assay. The obtained luminescence intensities from cell lysates were normalized to that from non-treated control cells. Results are shown as mean ± SEM ($n = 6$, $^{*}p < 0.05$, $^{**}p < 0.01$).

The gene silencing efficiency of hybrid micelles was determined to elucidate the effect of endosome-escaping functionality of CCPs on the ultimate biological activity of siRNA. The hybrid micelles prepared with a target sequence of siRNA (siLuc) or a control sequence (siCon)

were incubated with SKOV3-Luc cells at 50×10^{-9} M siRNA for 48 h, followed by a luciferase assay of the cell lysates (Figure 4). The siLuc/CCP-loaded micelles (i.e., PMM and ACO micelles) achieved significantly lower luciferase activity compared to the siLuc/nonCCP-loaded micelles (i.e., CAR micelles), indicating the greater gene silencing efficiency of hybrid micelles equipped with CCPs. The PMM micelles revealed further improved efficiency in gene silencing compared to the ACO micelles. Considering the similar cellular internalization behaviors of the three hybrid micelles (Figure 3A), it is reasonable to conclude that the greater gene silencing efficiency of the PMM hybrid micelles is mainly due to their improved capability of translocating siRNA payloads from endosomal compartment to cytosol based on their prominent charge-conversion functionality (Figure 3B). It should be noted that the significant difference in relative luciferase activity was observed between siLuc-loaded and siCon-loaded micelles and also that the PMM micelles did not affect the viability of SKOV3-Luc cells under the same condition as the gene silencing assay (Figure S8, Supporting Information). These results confirm the sequence-specific gene silencing effect of siLuc-loaded hybrid micelles.

4. Conclusions

In this study, PEG–PAsp(DET–PMM) was synthesized by utilizing PMM amide, which was more sensitive to acid hydrolysis compared to the previously developed ACO amide. The obtained PEG–PAsp(DET–PMM) successfully formed siRNA-loaded hybrid micelles having the size of ≈70 nm. The PMM micelles were stable in the 10% FBS-containing medium at least for 24 h, leading to the efficient cellular uptake of siRNA in cultured SKOV3-Luc cells, similar to ACO micelles. Ultimately, the PMM micelles achieved the greater gene silencing activity in the cells, compared to ACO micelles, presumably due to the more efficient endosomal escape of the siRNA payload by PEG–PAsp(DET-PMM). These results demonstrate that the fine-tuning of endosome-disrupting polymers improves the delivery efficacy of siRNA nanocarriers for enhanced gene silencing activity.

Supporting Information

Supporting Information is available from the Wiley Online Library or from the author.

Acknowledgements: This research was funded by JSPS through the "Funding Program for World-Leading Innovative R&D on Science and Technology (FIRST Program)", JST through Center of Innovation (COI) and Adaptable and Seamless Technology Transfer Program through Target-driven R&D (A-STEP), National Institute of Biomedical Innovation (NIBIO), and the Japanese Ministry of Health, Labour and Welfare through Grants-in-Aid for Scientific Research. Part of this work was conducted in the Research Hub for Advanced Nano Characterization, The University of Tokyo, supported by the Ministry of Education, Culture, Sports, Science and Technology (MEXT), Japan. The authors are grateful to A. Miyoshi for their assistance with experiments.

Received: January 24, 2014; Revised: March 3, 2014; Published online: April 8, 2014; DOI: 10.1002/marc.201400049

Keywords: calcium phosphate; poly(ethylene glycol); polymeric micelles; pH-responsive polymer; siRNA

[1] J. C. Burnett, J. J. Rossi, *Chem. Biol.* **2012**, *19*, 60.
[2] J. Gruenberg, F. G. van der Goot, *Nat. Rev. Mol. Cell Biol.* **2006**, *7*, 495.
[3] E. Wagner, *Acc. Chem. Res.* **2012**, *45*, 1005.
[4] O. Boussif, F. Lezoualc'h, M. A. Zanta, M. D. Mergny, D. Scherman, B. Demeneix, J. P. Behr, *Proc. Natl. Acad. Sci. USA* **1995**, *92*, 7297.
[5] Z. U. Rehman, D. Hoekstra, I. S. Zuhorn, *ACS Nano* **2013**, *7*, 3767.
[6] T. Bieber, W. Meissner, S. Kostin, A. Niemann, H. P. Elsasser, *J. Controlled Release* **2002**, *82*, 441.
[7] C. W. Evans, M. Fitzgerald, T. D. Clemons, M. J. House, B. S. Padman, J. A. Shaw, M. Saunders, A. R. Harvey, B. Zdyrko, I. Luzinov, G. A. Silva, S. A. Dunlop, K. S. Iyer, *ACS Nano* **2011**, *5*, 8640.
[8] S. M. Moghimi, P. Symonds, J. C. Murray, A. C. Hunter, G. Debska, A. Szewczyk, *Mol. Ther.* **2005**, *11*, 990.
[9] G. Grandinetti, N. P. Ingle, T. M. Reineke, *Mol. Pharm.* **2011**, *8*, 1709.
[10] N. Kanayama, S. Fukushima, N. Nishiyama, K. Itaka, W. D. Jang, K. Miyata, Y. Yamasaki, U. I. Chung, K. Kataoka, *ChemMedChem* **2006**, *1*, 439.
[11] K. Miyata, N. Nishiyama, K. Kataoka, *Chem. Soc. Rev.* **2012**, *41*, 2562.
[12] K. Masago, K. Itaka, N. Nishiyama, U.-I. Chung, K. Kataoka, *Biomaterials* **2007**, *28*, 5169.
[13] K. Miyata, M. Oba, M. Nakanishi, S. Fukushima, Y. Yamasaki, H. Koyama, N. Nishiyama, K. Kataoka, *J. Am. Chem. Soc.* **2008**, *130*, 16287.
[14] H. Uchida, K. Miyata, M. Oba, T. Ishii, T. Suma, K. Itaka, N. Nishiyama, K. Kataoka, *J. Am. Chem. Soc.* **2011**, *133*, 15524.
[15] Y. Lee, K. Miyata, M. Oba, T. Ishii, S. Fukushima, M. Han, H. Koyama, N. Nishiyama, K. Kataoka, *Angew. Chem. Int. Ed.* **2008**, *47*, 5163.
[16] F. Pittella, M. Zhang, Y. Lee, H. J. Kim, T. Tockary, K. Osada, T. Ishii, K. Miyata, N. Nishiyama, K. Kataoka, *Biomaterials* **2011**, *32*, 3106.
[17] F. Pittella, K. Miyata, Y. Maeda, T. Suma, S. Watanabe, Q. Chen, R. J. Christie, K. Osada, N. Nishiyama, K. Kataoka, *J. Controlled Release* **2012**, *161*, 868.
[18] F. Pittella, H. Cabral, Y. Maeda, P. Mi, S. Watanabe, H. Takemoto, H. J. Kim, N. Nishiyama, K. Miyata, K. Kataoka, *J. Controlled Release***2014**, *178*, 18.
[19] A. Tabaković, M. Kester, J. H. Adair, *WIREs Nanomed. Nanobiotechnol.* **2012**, *4*, 96.
[20] W. A. Blattler, B. S. Kuenzi, J. M. Lambert, P. D. Senter, *Biochemistry* **1985**, *24*, 1517.
[21] D. B. Rozema, K. Ekena, D. L. Lewis, A. G. Loomis, J. A. Wolff, *Bioconjugate Chem.* **2003**, *14*, 51.
[22] R. L. Juliano, X. Ming, O. Nakagawa, *Bioconjugate Chem.* **2012**, *23*, 147.
[23] K. Buyens, M. Meyer, E. Wagner, J. Demeester, S. C. De Smedt, N. N. Sanders, *J. Controlled Release* **2010**, *141*, 38.

Biomaterials 35 (2014) 5359–5368

Contents lists available at ScienceDirect

Biomaterials

journal homepage: www.elsevier.com/locate/biomaterials

Optimized rod length of polyplex micelles for maximizing transfection efficiency and their performance in systemic gene therapy against stroma-rich pancreatic tumors

Anjaneyulu Dirisala [a], Kensuke Osada [a,e,*], Qixian Chen [b], Theofilus A. Tockary [b], Kaori Machitani [b], Shigehito Osawa [b], Xueying Liu [c], Takehiko Ishii [a], Kanjiro Miyata [c], Makoto Oba [d], Satoshi Uchida [c], Keiji Itaka [c], Kazunori Kataoka [a,b,c,**]

[a] Department of Bioengineering, Graduate School of Engineering, The University of Tokyo, 7-3-1 Hongo, Bunkyo-ku, Tokyo 113-8656, Japan
[b] Department of Materials Engineering, Graduate School of Engineering, The University of Tokyo, 7-3-1 Hongo, Bunkyo-ku, Tokyo 113-8656, Japan
[c] Division of Clinical Biotechnology, Center for Disease Biology and Integrative Medicine, Graduate School of Medicine, The University of Tokyo, 7-3-1 Hongo, Bunkyo-ku, Tokyo 113-0033, Japan
[d] Department of Molecular Medicinal Sciences, Division of Pharmaceutical Chemistry, School of Pharmaceutical Sciences, Nagasaki University, 1-14 Bunkyo-machi, Nagasaki 852-8521, Japan
[e] Japan Science and Technology Agency, PRESTO, 4-1-8 Honcho, Kawaguchi, Saitama 332-0012, Japan

ARTICLE INFO

Article history:
Received 19 February 2014
Accepted 16 March 2014
Available online 8 April 2014

Keywords:
DNA
Micelle
Nanoparticle
Gene transfer
In vitro test
In vivo test

ABSTRACT

Poly(ethylene glycol) (PEG) modification onto a gene delivery carrier for systemic application results in a trade-off between prolonged blood circulation and promoted transfection because high PEG shielding is advantageous in prolonging blood retention, while it is disadvantageous with regard to obtaining efficient transfection owing to hampered cellular uptake. To tackle this challenging issue, the present investigation focused on the structure of polyplex micelles (PMs) obtained from PEG–poly(L-lysine) (PEG–PLys) block copolymers characterized as rod-shaped structures to seek the most appreciable formulation. Comprehensive investigations conducted with particular focus on stability, PEG crowdedness, and rod length, controlled by varying PLys segment length, clarified the effect of these structural features, with particular emphasis on rod length as a critical parameter in promoting cellular uptake. PMs with rod length regulated below the critical threshold length of 200 nm fully exploited the benefits of cross-linking and the cyclic RGD ligand, consequently, exhibiting remarkable transfection efficiency comparable with that of ExGen 500 and Lipofectamine® LTX with PLUS™ even though PMs were PEG shielded. The identified PMs exhibited significant antitumor efficacy in systemic treatment of pancreatic adenocarcinoma, whereas PMs with rod length above 200 nm exhibited negligible antitumor efficacy despite a superior blood circulation property, thereby highlighting the significance of controlling the rod length of PMs to promote gene transduction.

1. Introduction

Significant advances in the development of smart nano-devices constructed by exploiting material-based molecular design concepts have dramatically improved medical diagnosis and treatment [1–4]. One of their intriguing application is gene therapy, which has emerged as a potential tool for treating intractable diseases [5,6] by means of transducing therapeutic proteins, because this needs an appropriate delivery system that transports inherently fragile DNA in biological milieu to pathological sites and enters into the cells for expressing therapeutic proteins [7,8]. To establish this therapeutic concept, through systemic administration, the property of blood retention for increasing delivery efficiency to the targeted sites is an essential prerequisite along with gene transfection capability [7,8]. The primary property of a gene delivery system for systemic application is to securely package DNA

* Corresponding author. Department of Bioengineering, Graduate School of Engineering, The University of Tokyo, 7-3-1 Hongo, Bunkyo-ku, Tokyo 113-8656, Japan. Tel.: +81 3 5841 1654; fax: +81 3 5841 7139.
** Corresponding author. Department of Materials Engineering, Graduate School of Engineering, The University of Tokyo, 7-3-1 Hongo, Bunkyo-ku, Tokyo 113-8656, Japan. Tel.: +81 3 5841 7138; fax: +81 3 5841 7139.
E-mail addresses: osada@bmw.t.u-tokyo.ac.jp (K. Osada), kataoka@bmw.t.u-tokyo.ac.jp (K. Kataoka).

http://dx.doi.org/10.1016/j.biomaterials.2014.03.037
0142-9612/

within the delivery system and to inhibit nonspecific interactions with biological components, including opsonins, in addition to nuclease tolerability [9]. In view of these requirements, we have developed a poly(ethylene glycol) (PEG)-shielded gene delivery system, polyplex micelles (PMs), as a promising formulation constructed on the basis of the self-assembly of PEG–polycation block copolymers and plasmid DNA (pDNA) [10,11]. Following this electrostatic complexation, pDNA is packaged into a distinct rod-shaped bundle composed of pDNA folded several times [12] as the core compartment and the PEG chains surrounding it as the protective shell compartment. This characteristic structure of PMs enables systemic applications [13]. However, the blood retention property of the firstly developed PMs was unsatisfactory to obtain a sufficient therapeutic effect via systemic administration; thus, modifications were required to reinforce PM stability in the bloodstream. For this purpose, the introduction of a disulfide cross-linking into the core compartment [14] for preventing disassembly was an effective strategy, as evidenced by the cross-linked PEG–poly(L-lysine) (PEG–PLys) block copolymer-based PMs indeed exhibiting prolonged blood circulation [15,16].

Besides the cross-linking, the PEG compartment also substantially contributes in promoting blood circulation. A recent study highlighting the role of the PEG compartment described the importance of increasing PEG crowdedness in prolonging the blood retention period: higher PEG crowdedness on PMs prepared from a lower degree of polymerization (DP) of the PLys segment of PEG–PLys led to a better blood circulation property [17]. Moreover, PMs of lower PLys DP exhibited increased transcription efficiency [18]. These studies suggested that cross-linked PMs prepared from lower PLys DP would be a suitable formulation for systemic application. However, with regard to the transfection activity, highly PEG-shielded PMs may in turn be disadvantageous because the reduced affinity of these PMs with the cellular membrane may result in precluded cellular uptake. In addition, we found that PLys DP affects the folding number of pDNA [18] within the PM core; PMs prepared from lower PLys DP result in a longer rod length by less folded pDNA. Indeed, PMs prepared from PLys DP 20 displayed rod length ranging several hundred nanometers, while those prepared from PLys DP 70 displayed rod length around 70 nm [17,18]. Such long PMs with several hundred nanometer-sized particles may unlikely be uptake efficiently compared with that of short PMs [19]. Furthermore, a relatively lower binding affinity of PEG–PLys of lower PLys DP to pDNA than that of PEG–PLys of higher PLys DP [20] may decrease the structural stability of PMs, thereby influencing transfection efficiency. Although such impaired stability and unfavorable character for cellular uptake may be improved by applying cross-linking [14] and the ligand molecules [21–24], the inherent structural features of PMs prepared from lower PLys DP may suggest their disadvantageous property in obtaining efficient transfection. Eventually, a concern may arise that the achievement of PMs arriving at target sites by the end of a long systemic journey may result in precluded transfection. These arguments raise the need of a comprehensive study taking each structural feature into consideration for obtaining an ultimate PM formulation. Therefore, the present study aimed to seek the most appreciable formulation to maximize the transfection efficiency on a basis of precise structural control of PMs by varying PLys DP, with particular focus on structural stability [20], PEG crowdedness [17], and rod length [17,18], for completely utilizing the benefits of cross-linking [14–16] and the cyclic RGD (Arg–Gly–Asp) (cRGD) peptide as a ligand for specific integrin-mediated uptake [21–24].

The present study clarified the effect of the abovementioned structural features on cellular uptake and revealed the presence of critical rod length for efficient cellular uptake, consequently identifying the most appreciable PM formulation to promote transfection efficiency. Taking the advantages of the cross-linking and the cRGD ligand upon systemic application to provide stability and tumor homing, respectively, the PM formulation was challenged to systemic treatment of one of the most intractable solid tumor, pancreatic adenocarcinoma, with stroma-rich characteristics, thereby validating the significance of careful control of PM structure, particularly rod length, for promoting systemic gene transfection.

Table 1
Chemical characterization of a series of PEG–PLys with varying PLys DP.

Block copolymers	PLys DP	M_w/M_n[a]	Conjugation ratio of SH in Lys (%)[b]	Conjugation ratio of cRGD to PEG–PLys (%)[c]
PEG–PLys20	20	1.04	0	0
PEG–PLys42	42	1.04	0	0
PEG–PLys69	69	1.05	0	0
PEG–PLys20(SH)	20	1.04	10	0
PEG–PLys42(SH)	42	1.04	12	0
PEG–PLys69(SH)	69	1.05	12	0
R–PEG–PLys21	21	1.03	0	92
R–PEG–PLys41	41	1.05	0	84
R–PEG–PLys69	69	1.06	0	84
R–PEG–PLys21(SH)	21	1.03	12	85
R–PEG–PLys41(SH)	41	1.05	13	80
R–PEG–PLys69(SH)	69	1.06	13	83

[a] Determined from GPC equipped with the TOSOH HLC-8220 column calibrated with commercial PEG standards.
[b] Introducing ratio of thiol (SH) groups against ε-NH_2 groups of lysine units of either MeO PEG–PLys or acetal–PEG–PLys determined from ^{1}H NMR spectra.
[c] Conjugation ratio of cRGD ligand onto α-end of either acetal–PEG–PLys or acetal–PEG–PLys(SH) determined from ^{1}H NMR spectra.

2. Materials and methods

2.1. Materials

α-Methoxy-ω-amino-PEG (MeO–PEG) and α-acetal-ω-amino-PEG (acetal–PEG) of M_w 21 kDa were obtained from NOF Co., Ltd. (Tokyo, Japan). N^{ε}-trifluoroacetyl-L-lysine *N*-carboxyanhydride [Lys(TFA)–NCA] was synthesized as reported previously [25]. *N*-succinimidyl 3-(2-pyridyldithio)-propionate (SPDP) and Slide-a-lyzer dialysis cassettes (MWCO = 3.5 kDa) were purchased from Thermo Scientific (Rockford, IL). Cyclo[RGDfK(C-ε-Acp)] (cRGD) peptide (ε-Acp: 6-aminocaproic acid) was purchased from Peptide Institute Inc. (Osaka, Japan). Luciferase (Luc)-encoding gene-inserted pCAcc vector having the CAG promoter (pCAG–Luc2: 6477 bp) was obtained from RIKEN Gene Bank (Tsukuba, Japan). pDNA encoding human soluble form of vascular endothelial growth factor receptor-1 (VEGFR-1) (or soluble fms-like tyrosine kinase-1: sFlt-1) with pCAcc vector having the CAG promoter (pCAG–sFlt-1: 7186 bp) was constructed according to a previously described method [15]. Both pCAG–Luc2 and pCAG–sFlt-1 were transformed into competent *Escherichia coli* DH5α cells and amplified, following which endotoxin-free pDNAs were obtained using the NucleoBond® Xtra Maxi EF Kit (Macherey–Nagel GmbH & Co., Germany). The other pDNAs, pKF18 (2204 bp) and pAUR316 (11,613 bp), were purchased from Takara Bio Inc. (Otsu, Japan). pDNAs were labeled with Cy5 using the Label IT® Tracker™ Intracellular Nucleic Acid Localization Kit obtained from Mirus Bio Corp. (Madison, WI) according to the manufacturer's instructions and used for studying cellular uptake. Dulbecco's modified eagle's medium (DMEM) and Dulbecco's phosphate-buffered saline (DPBS) were purchased from Sigma–Aldrich Co. (Madison, WI). Fetal bovine serum (FBS) was purchased from Dainippon Sumitomo Parma Co., Ltd. (Osaka, Japan). Cell culture lysis buffer and Luciferase Assay System Kit were purchased from Promega Co. (Madison, WI). Micro BCA™ Protein Assay Reagent Kit was purchased from Pierce Co., Inc. (Rockford, IL). ExGen 500 (linear 22-kDa polyethylenimine) and Lipofectamine® LTX with PLUS™ reagent were purchased from MBI Fermentas Co. (Burlington, ON, Canada) and Invitrogen Life Technologies Corp. (Carlsbad, CA), respectively. Rat monoclonal antibody against mouse platelet endothelial cell adhesion molecule-1 (PECAM-1) was purchased from Santa Cruz Biotechnology Inc. (Santa Cruz, CA). Alexa 488-conjugated (A11006), Alexa 647-conjugated (A21247) goat anti-rat, and Alexa 488-conjugated (A11008) goat anti-rabbit IgG (H + L) secondary antibodies were obtained from Invitrogen Molecular Probes (Eugene, OR). Rabbit monoclonal antibody against mouse VEGF receptor-1 [Y103] (ab32152) was purchased from Abcam (Tokyo, Japan). Human epithelial ovarian carcinoma cells (HeLa) and human pancreatic adenocarcinoma-BxPC3 cells were obtained from the American Type Culture Collection (ATCC, Manassas, VA). BALB/c-nu/nu mice (female, 5-weeks old) were purchased from Charles River Laboratories (Tokyo, Japan). All animal experimental procedures were performed in

compliance with the Guidelines for the Care and Use of Laboratory Animals as stated by the Animal Committee of the University of Tokyo.

2.2. Synthesis of PEG-block copolymers

2.2.1. Synthesis of PEG–PLys

A series of MeO–PEG–PLys block copolymers with varying PLys DP were synthesized according a previously reported procedure [18]. In brief, Lys(TFA)–NCA was conjugated onto the ω-NH_2 terminal group of MeO–PEG via ring-opening polymerization in N,N-dimethylformamide containing 1 M thiourea. It should be noted that 21-kDa PEG was used in the present study instead of 12-kDa PEG [21,22] and 17-kDa PEG used previously [16,23] because we found that the cRGD ligand effect was particularly pronounced for PMs with high PEG shielding [23,24]. The molecular weight distribution (M_w/M_n) of a series of MeO–PEG–PLys(TFA) was determined to be ≤1.05 (Table 1) from gel permeation chromatography (GPC) equipped with TOSOH HLC-8220 calibrated with varying M_w of commercial PEG standards. Following this, MeO–PEG–PLys(TFA) was dissolved in methanol containing 1 N NaOH to remove protective TFA groups at 35 °C for 6 h. PLys DP was determined to be 20, 42, and 69 by comparing the peak intensity ratio of the methylene protons of PEG [$(CH_2)_2O$, $\delta = 3.7$ ppm] to the β-, γ-, and δ-methylene protons of lysine [$(CH_2)_3$, $\delta = 1.3$–1.9 ppm] units from the ^{1}H NMR spectra, respectively. A series of acetal–PEG–PLys with varying PLys DP was also synthesized similarly. M_w/M_n of a series of acetal–PEG–PLys(TFA) with varying PLys DP was determined to be ≤1.06 from GPC (Table 1). PLys DP was determined to be 21, 41, and 69 from the ^{1}H NMR spectra.

2.2.2. Synthesis of thiolated PEG–PLys [PEG–PLys(SH)]

PEG–PLys(SH) polymers were synthesized by conjugating pyridyldithiopropionyl (PDP) groups onto the ε-amino groups of lysine units of the PLys segment of PEG–PLys using the heterobifunctional reagent *N*-succinimidyl 3-(2-pyridyldithio) propionate (SPDP), as reported previously [14]. In brief, MeO–PEG–PLys composed of 21-kDa PEG and PLys69 (50 mg, 1.55 μmol) was dissolved in 2 ml of *N*-methyl-2-pyrrolidone (NMP) supplemented with 5 wt% LiCl and reacted with SPDP (5 mg, 16 μmol) pre-dissolved in NMP containing *N,N*-diisopropylethylamine (10 mol excess against SPDP) at room temperature (RT). After 4 h of stirring, the reaction was terminated by precipitation into diethyl ether. The precipitated polymer was then dissolved in 0.01 N HCl, dialyzed against the distilled water, and lyophilized to obtain MeO–PEG–PLys(PDP). A series of acetal–PEG–PLys(PDP) with varying PLys DP was also synthesized similarly and further used for cRGD ligand conjugation. The introduction ratio of thiol groups was determined from the ^{1}H NMR spectrum recorded in DCl containing D_2O (pD = 2.4) at 25 °C by the peak intensity ratio of the β-, γ-, and δ-methylene protons of lysine [$(CH_2)_3$, $\delta = 1.3$–1.9 ppm] units to the pyridyl protons of the 3-(2-pyridyldithio) propionyl group (C_5H_4N, $\delta = 7.2$–8.3 ppm). The degree of thiol group substitution was determined to be 10%–13% for all polymers (Table 1). PEG–PLys(SH) was obtained by treating PEG–PLys(PDP) with dithiothreitol (DTT).

2.2.3. Synthesis of cRGD–PEG–PLys and cRGD–PEG–PLys(SH)

The cyclo[RGDfK(C-ε-Acp)] (cRGD) peptide ligand was conjugated onto the α-end of acetal–PEG–PLys through the formation of a thiazolidine ring between the *N*-terminal cysteine of the cRGD peptide and the aldehyde group generated in acetal–PEG–PLys following incubation at acidic pH, as reported previously [21]. In brief, acetal–PEG–PLys of PLys69 (50 mg, 1.55 μmol) was dissolved in 2 ml of 10 mM HEPES buffer (pH 7.4) and dialyzed against 0.01 N HCl (pH 2.0) to yield aldehyde from the acetal group. The pH of the dialyzed solution was adjusted to 5.0 by 0.01 N NaOH, following which the pre-DTT-treated cRGD (1.5 mg, 1.62 μmol) solution was added dropwise while stirring. After stirring overnight at 25 °C, the polymer solution was dialyzed against HEPES with 150 mM NaCl, followed by distilled water, and then lyophilized to obtain cRGD–PEG–PLys. A series of cRGD–PEG–PLys(SH) block copolymers with varying PLys DP were also synthesized similarly, as described above, with pre-DTT treatment. The percentage of cRGD conjugation was determined by the peak intensity ratio of benzyl protons (D-phenyl alanine, f: D-Phe; $\delta = 7.3$–7.4 ppm) of the cRGD peptide to the methylene protons of PEG ($\delta = 3.7$ ppm) from the ^{1}H NMR spectra, and the conjugation ratio was calculated to be 80%–92% for all polymers (Table 1).

2.3. Preparation of PMs

A series of PEG–PLys with varying PLys DP and pDNA were separately dissolved in 10 mM HEPES (pH 7.4). Noncross-linked PMs (non-CPMs) were simply prepared by fast mixing 1-unit volume of the PEG–PLys solution with 2-unit volume of pDNA solution at the N/P ratio of 2. The N/P ratio is defined as the residual molar ratio of amine (N) groups of PEG–PLys to the phosphate (P) groups of pDNA. It should be noted that cross-linked PMs (CPMs) were prepared from PEG–PLys(SH) polymers as reported previously [14]. In brief, a series of PEG–PLys(SH) with varying PLys DP was dissolved in 100 mM DTT containing 10 mM HEPES (pH 7.4) and incubated for 4 h at RT to cleave any undesired preliminary formation of disulfide bonds. PMs were then prepared at the N/P ratio of 2 by fast mixing the pre-DTT treated PEG–PLys(SH) solution with the pDNA solution. After overnight incubation at RT, PM solutions were transferred to dialysis cassettes and dialyzed against 0.5% dimethyl sulfoxide (DMSO) containing HEPES for a day, followed by additional dialysis against only HEPES at RT for 2 days to remove DTT and DMSO from the PM solutions. DMSO added to the dialysis buffer facilitates the formation of disulfide cross-links between PEG–PLys(SH) polymers because it is an oxidizing agent for thiol (SH) groups [26]. The CPM solutions were recovered from dialysis cassettes and checked for pDNA concentration in each micelle solution by measuring UV absorption at 260 nm using NanoDrop ND-1000 (NanoDrop Technologies Inc., Rockland, DE) to confirm that the process of dialysis did not affect the concentration of pDNA of PMs. PMs without and with cross-linking were abbreviated as PEG–PLys and PEG–PLys(SH), respectively. CPMs equipped with the cRGD ligand were abbreviated as R–PEG–PLys(SH).

2.4. Preparation of transfection complexes from ExGen 500 and Lipofectamine® LTX with PLUS™

Polyplexes based on ExGen 500 were formulated according to the manufacturer's protocol at the recommended N/P ratio of 6. In brief, 3.3 μl of ExGen 500 was added to 100 μl of pCAG–Luc2 DNA (10 ng/μl) and immediately vortexed for 10 s. After 30 min of incubation at RT, the polyplex solution containing 1 μg of pDNA was directly added to the cells in DMEM containing 10% FBS to evaluate their transfection efficacy. In addition, lipoplexes based on Lipofectamine® LTX with PLUS™ were prepared according to the manufacturer's protocol. In brief, 1 μl of PLUS™ reagent containing 50 μl of Opti-MEM® medium with 1 μg of pCAG–Luc2 DNA and 5 μl of Lipofectamine® LTX containing 50 μl of Opti-MEM® were prepared simultaneously. Lipoplexes were obtained by mixing these two solutions at a 1:1 v/v ratio. After 5 min of incubation at RT, 1 μg of pDNA containing the lipoplex solution was directly added to the cells in DMEM containing 10% FBS to evaluate their transfection efficacy.

2.5. Transmission electron microscopy (TEM) characterization

The morphology of PMs was observed using the H-7000 TEM machine (Hitachi Ltd., Tokyo, Japan) operated at an acceleration voltage of 75 kV, as reported previously [18]. In brief, copper TEM grids (Nisshin EM Corp., Japan) containing carbon-coated collodion membrane were glow-discharged for 30 s using an Eiko IB-3 ion coater (Eiko Engineering Co., Ltd., Japan) for hydrophilization. The hydrophilized grids were immersed into uranyl acetate (UA) (2% w/v)-treated PM solutions for 30 s to achieve effective staining. The sample-deposited grids were blotted onto the filter paper to remove excess solution, followed by air-drying for 30 min. Following this, the grids were transferred to the TEM machine for imaging. Rod lengths were obtained by measuring the major axis length of folded pDNA (appeared as rod-shaped structures) from the TEM images using Image J 1.45 software (National Institutes of Health, USA), and more than 100-rod structures were measured to plot the rod length distribution of each PM. It should be noted that the PEG shell of PMs was not observed owing to low affinity of UA.

2.6. Cellular uptake of PMs by flow cytometry

HeLa cells were seeded onto 12-well culture plates (50,000 cells/well) with 500 μl of DMEM containing 10% FBS and 1% antibiotics (penicillin and streptomycin) and incubated in a humidified atmosphere supplemented with 5% CO_2 at 37 °C. After 24 h of incubation, the medium was replaced with fresh medium. The cells were then treated with PM solutions (1 μg of Cy5-labeled pDNA/well) and incubated for 24 h. The medium was removed, cells were then washed three times with ice-cold DPBS to remove extracellular fluorescence, and cells were detached by trypsin–EDTA treatment. Trypsinized cells were then harvested from the cell culture plate and resuspended in 1 ml of ice-cold DPBS. After filtering the cells through a nylon mesh, the cells were analyzed by a BD™ LSR II flow cytometer equipped with FACS-Diva™ software (BD Biosciences, Franklin Lakes, NJ) to measure the fluorescence intensity of internalized pDNA. The obtained data were expressed as the mean fluorescence intensity from three independent samples ($n = 3$).

2.7. Evaluation of in vitro transfection efficiency

HeLa cells were seeded onto 24-well culture plates (20,000 cells/well) with 400 μl of DMEM containing 10% FBS and 1% antibiotics (penicillin and streptomycin) and incubated for 24 h in a humidified atmosphere supplemented with 5% CO_2 at 37 °C. After exchanging the medium with a fresh one, 1 μg of pCAG–Luc2 DNA containing PM solutions was added to each well. After 24 h of incubation, the medium was exchanged with 400 μl of fresh medium, followed by another 24 h of incubation. The cells were then washed three times with 400 μl of ice-cold DPBS and lysed by 150 μl of cell culture lysis buffer at 37 °C for 15 min. Immediately, 20 μl of the cell lysate was transferred to a 96-well luminometry plate, followed by the addition of 100 μl of Luciferase Assay Reagent (Promega, Madison, WI) to each well, and allowed to react for 15 min. The Luc expression was then measured for 10 s from the photoluminescence intensity using Mithras LB 940 (Berthold Technologies, Bad Wildbad, Germany). The amount of total protein in the cell lysate was quantified using the Micro BCA™ Protein Assay Kit (Pierce, Rockford, IL), and the obtained Luc activity was normalized against the corresponding amount of total protein in the cell lysates. The transfection efficiency of polyplexes from ExGen 500 and lipoplexes from Lipofectamine® LTX with PLUS™ was simultaneously evaluated with the same concentration of pCAG–Luc2 DNA (1 μg of pDNA/well). The data were expressed as relative light units (RLU) per mg of protein (RLU/mg protein) ($n = 6$).

2.8. Evaluation of transfection-mediated cytotoxicity

HeLa cells were plated onto 24-well culture dishes (20,000 cells/well) in 400 μl DMEM containing 10% FBS and 1% antibiotics (penicillin and streptomycin) and incubated in a humidified atmosphere with 5% CO_2 at 37 °C. After 24 h of incubation, the medium was replaced with 400 μl of fresh medium, followed by the addition of CPMs of R–PEG–PLys69(SH), polyplexes of ExGen 500, and lipoplexes of Lipofectamine® LTX with PLUS™ solutions equivalent to 1 μg of pDNA/well. After 24 h of incubation, the medium was replaced with fresh medium, followed by another 24 h of incubation. The cells were washed three times with ice-cold DPBS, followed by the addition of 200 μl of fresh medium. Cell viability was assessed on the basis of 2-(2-methoxy-4-nitrophenyl)-3-(4-nitrophenyl)-5-(2,4-disulfophenyl)-2*H*-tetrazolium (WST-8) reduction to WST-8 formazan by the dehydrogenase activity of viable cells using the Cell Counting Kit-8 (CCK-8) (Dojindo, Kumamoto, Japan) according to the manufacturer's instructions. In brief, 20 μl of the CCK-8 reagent was added to each well and allowed to develop orange-colored WST-8 formazan for 2 h. The UV absorbance of WST-8 formazan in each well was quantified at 450 nm using a microplate reader (Model 680, Bio-Rad, UK). The cell toxicity was expressed as the percentage of cell viability normalized against control cells treated with 10 mM HEPES (pH 7.4) ($n = 6$).

2.9. In vivo tumor growth suppression

BxPC3 cells (100 μl of 1×10^7 cells/ml in DPBS) derived from human pancreatic adenocarcinoma were subcutaneously inoculated into BALB/c-nu/nu mice (female, 6-weeks old) to develop xenografts and allowed to grow until they reached a proliferative phase. Once the tumor volume reached approximately 75 mm^3, PMs loading either pCAG–sFlt-1 or pCAG–Luc2 DNA (20 μg in 200 μl of 10 mM HEPES containing 150 mM NaCl) were intravenously injected into the tail vein three times at a 4-day interval (days 0, 4, and 8). It should be noted that PM loading pCAG–Luc2 DNA containing the non-therapeutic gene was used as a control. The tumor size was measured over time using a digital vernier caliper across its longest longitudinal diameter (a) and longest transverse diameter (b), and the tumor volume (V) was calculated using the following equation: $V = 0.5\ ab^2$. The measurement of tumor size was terminated on day 27 in compliance with the guidelines for animal experiments because the tumors of the control group showed ulcer characteristics. The relative tumor volume (V/V_0) was calculated against the tumor volume at day 0 (V_0) ($n = 4$). Day 0 was the first day of PM injection for treatment.

2.10. Quantification of sFlt-1 protein expression at the tumor site

PMs loading pCAG–sFlt-1 DNA (20 μg in 200 μl of 10 mM HEPES containing 150 mM NaCl) were intravenously injected once into the tumor-bearing mice via the tail vein. The mice were sacrificed after 48 h of injection and xenografted tumors were excised, placed into tissue-Tek-OCT, frozen at −80 °C for 2 days, and sectioned into 10-μm-thick slices with a rotary microtome maintained in a cryostat at −20 °C, following which they were transferred onto a microscopic slide. The expressed sFlt-1 protein was immunofluorescent-stained by rabbit monoclonal antibody against mouse VEGF receptor-1 [Y103] (ab32152) (Abcam, Tokyo, Japan), followed by incubation with Alexa Fluor 488-conjugated goat anti-rabbit IgG (H + L) secondary antibody (A11008) (Invitrogen, Carlsbad, CA). VECs of the tumor vasculature were immunofluorescent-stained by rat monoclonal antibody against mouse PECAM-1, followed by incubation with Alexa Fluor 647-conjugated goat anti-rat IgG (H + L) secondary antibody (A21247) (Invitrogen, Carlsbad, CA). The nuclei were fluorescent-stained with Hoechst 33342 (H3570) (Invitrogen, Carlsbad, CA). The immunofluorescent-stained tumor sections were analyzed for fluorescence using a confocal laser scanning microscope (CLSM), LSM 780 (Carl Zeiss, Oberkochen, Germany). The sFlt-1 gene expression was quantified by measuring the integrated density of Alexa-488 fluorescence per image with 6 images for each sample from the CLSM images using Image J 1.45 software.

2.11. Quantification of vascular density in the tumors

PMs loading pCAG–sFlt-1 DNA (20 μg in 200 μl of 10 mM HEPES containing 150 mM NaCl) were intravenously administered to the tumor-bearing mice via the tail vein three times at a 4-day interval (days 0, 4, and 8). After 20 days, the mice were sacrificed and xenografted tumors were excised, placed into tissue-Tek-OCT, frozen at −80 °C for 2 days, and sectioned into 10-μm-thick slices with a rotary microtome maintained in a cryostat at −20 °C, followed which they were transferred onto a microscopic slide. VECs of the tumor vasculature were immunofluorescent-stained by rat monoclonal antibody against mouse PECAM-1, followed by incubation with Alexa Fluor 488-conjugated goat anti-rat IgG (H + L) secondary antibody (A11006) (Invitrogen, Carlsbad, CA). The immunofluorescent-stained tumor cryosections were analyzed for fluorescence by LSM 780. The vascular density was quantified by measuring the percentage area of PECAM-1-positive green pixels per image with 6 images for each sample from the CLSM images using Image J 1.45 software.

3. Results and discussion

3.1. Cellular uptake of PMs without core cross-linking

The effect of PLys DP (20, 42, and 69) on cellular uptake was initially examined. PMs prepared from a series of PEG–PLys with varying PLys DP and fluorescent-labeled pCAG–Luc2 DNA (6477 bp) were used to evaluate the cellular uptake efficiency of HeLa cells by measuring the intracellular fluorescence intensity using flow cytometry. As presented in Fig. 1a, cellular uptake was highly dependent on PLys DP of PEG–PLys; higher cellular uptake was observed for higher PLys DP, whereas lower cellular uptake was observed for lower PLys DP, in accordance with our previous report on PMs with PLys DP ranging from 7 to 48 [27]. In order explore the underlying effect of PLys DP on cellular uptake, the stability of PMs in the culture medium and polyanionic environment was examined because these two factors may interfere the level of cellular uptake efficiency because of following reasons: the culture medium supplemented with 10% FBS includes nucleases [28] and the cell membrane contains negatively charged extracellular glycosaminoglycans (GAGs) [29,30], which can potentially destabilize PMs through polyion exchange reactions. The stability in the culture medium was evaluated by observing the intactness of pDNA through quantitative real-time polymerase chain reaction (qRT-PCR). pDNA within PMs showed almost no digestion regardless of PLys DP, whereas naked pDNA was rapidly digested (Fig. S1). This observation indicated that PMs were stable enough in the culture medium regardless of PLys DP, thereby implying another possibility occurring on the cell membrane. It should be noted that previous reports suggested that GAGs, particularly heparan sulfate (HS), could destabilize electrostatically driven self-assembled polymeric and liposomal gene delivery systems [31,32]. Thus, the tolerability of PMs to HS dissociation was evaluated by observing the release of pDNA on agarose gel electrophoresis, with a note that HS is the most abundant [29,30] and sulfated (0.9 sulfate per repeating disaccharide unit) [33] GAG among all other extracellular GAGs present on the cell membrane. Indeed, HS dissociated PMs regardless of PLys DP at high concentrations (6 mg/ml). Noteworthy was that at mid-range concentrations (1–4 mg/ml), there is a trend showing that the tolerability was progressively increased with the increase in PLys DP. The highest PLys DP showed better tolerability than the lowest PLys DP (Fig. S2a). This difference in tolerability may be accountable for the trend of cellular uptake of different PLys DP (Fig. 1a), such that less stable PMs of PEG–PLys20 were susceptible to disassembly at the cellular membrane, thereby resulting in lower cellular uptake. The possibility of HS as a barrier for cellular uptake was examined by further evaluation using HeLa cells treated with heparanase, an HS digestive enzyme, which can selectively remove extracellular HS [34]. The amount of uptake was indeed increased in heparanase-treated cells compared to that of cells without heparanase treatment (Fig. S3); yet there was only a limited increase in cellular uptake for PMs of PEG–PLys20.

3.2. Cellular uptake of CPMs

To further explore the precluded cellular uptake of PMs of PEG–PLys20, disulfide cross-linking was introduced in the core of PMs to stabilize the structure according to our previous procedure [14]. Thiol groups were introduced onto $-NH_2$ groups of lysine units of a series of PEG–PLys using the *N*-succinimidyl 3-(2-pyridyldithio) propionate (SPDP) reagent to obtain PEG–PLys(SH) for preparing CPMs. Here, the thiolation degree (Table 1) was chosen to be 10% on the basis of previous optimization in the *in vitro* gene expression assay [15]. It should be noted that the disulfide cross-links retain environmental responsiveness, providing remarkable stability in

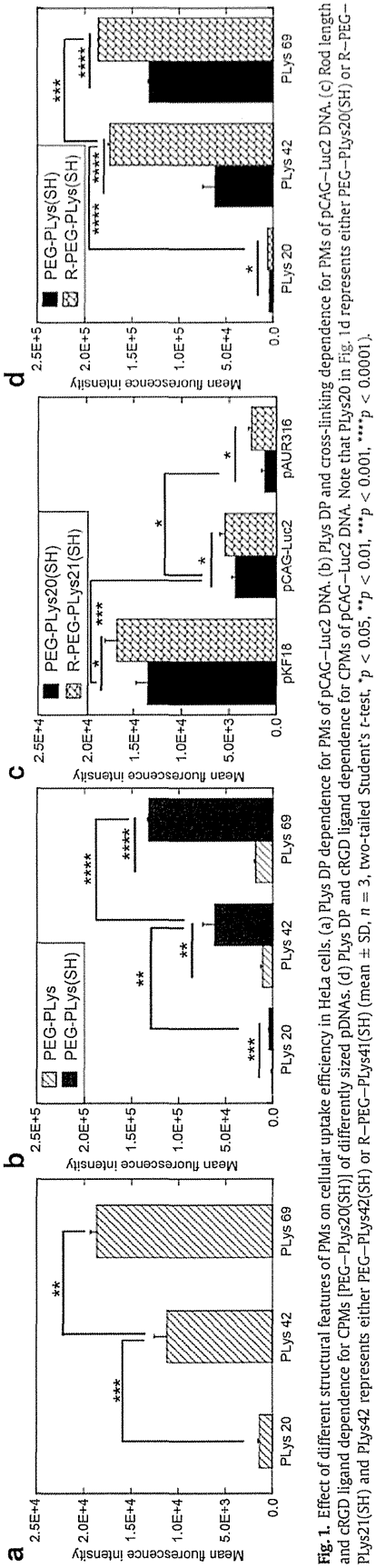

Fig. 1. Effect of different structural features of PMs on cellular uptake efficiency in HeLa cells. (a) PLys DP dependence for PMs of pCAG–Luc2 DNA. (b) PLys DP and cross-linking dependence for PMs of pCAG–Luc2 DNA. (c) Rod length and cRGD ligand dependence for CPMs [PEG–PLys20(SH)] of differently sized pDNAs. (d) PLys DP and cRGD ligand dependence for CPMs of pCAG–Luc2 DNA. Note that PLys20 in Fig. 1d represents either PEG–PLys20(SH) or R–PEG–PLys21(SH) and PLys42 represents either PEG–PLys42(SH) or R–PEG–PLys41(SH) (mean ± SD, $n = 3$, two-tailed Student's t-test, $^{*}p < 0.05$, $^{**}p < 0.01$, $^{***}p < 0.001$, $^{****}p < 0.0001$).

the extracellular milieu, whereas CPMs are liable to be cleaved in the intracellular reductive environment responding to high glutathione (10 mM) concentration, thereby triggering the release of encapsulated pDNA [14,35]. As anticipated, tolerability against HS treatment was significantly improved for all CPMs regardless of PLys DP, and no pDNA release from CPMs was observed in an electrophoretogram (Fig. S2b) even at the highest HS concentration (6 mg/ml) able to dissociate PMs without cross-linking (non-CPMs). Eventually, cellular uptake was significantly promoted by the introduction of disulfide cross-linking in all PLys DP (Fig. 1b). Nevertheless, the trend of PLys DP dependence persisted even after cross-linking. The CPMs of PEG–PLys20(SH) still exhibited significantly precluded cellular uptake compared with other PLys DP regardless of remarkably improved stability against HS, as shown by no release of pDNA in the electrophoretogram (Fig. S2b). Therefore, there should be other factors apart from an unfavorable dissociation that limit cellular uptake.

3.3. Effect of PEG density of PMs on their cellular uptake

We then focused on the different PEG density of these PMs with varying PLys DP; PMs with lower PLys DP are characterized by higher PEG density, whereas those with higher PLys DP are characterized by lower PEG density [17]. Accordingly, it is assumed that higher PEG density of PEG–PLys20 may account for lower cellular uptake as a result of reduced interactions with the cell membrane [36,37]. To clarify this assumption, PEG density of CPMs with different PLys DP needed to be quantitatively determined. Upon this demonstration, the binding number of tethered PEG to pDNA should be known [17]. However, its direct estimation was technically difficult for PEG–PLys(SH) within CPMs because Alexa Fluor-labeled polymers may interact with the dialysis membrane during the preparation process of CPMs; therefore, the binding number of block copolymers to pDNA may not be accurately quantified. Hence, we inferred the PEG density of CPMs from that of non-CPMs, considering that pDNA within PMs is packaged into a distinct rod-shaped structure (see Figs. S4 and S5 for representative structures) with specific rod length distribution based on the quantized folding scheme [12], and PMs with similar rod length distribution were assumed to retain similar PEG density because the rod length is a function of PEG density [17]. Thus, the rod length distributions of CPMs and non-CPMs of respective PLys DP were examined and found to exhibit almost a similar distribution (Fig. 2a–f). Accordingly, it may be reasonable to consider that the PEG density of CPMs of particular PLys DP was similar to that of non-CPMs. Moreover, direct PEG height observation from cryogenic TEM (cryo-TEM) indicated a similar PEG height for CPMs and non-CPMs at corresponding PLys DP (Table S1, Fig. S6a for representative cryo-TEM images), further supporting their similar PEG density. Thus, the PEG density of non-CPMs was calculated for different PLys DP using a previously reported method [17] and inferred to CPMs of corresponding PLys DP (Table S2), giving the values of 0.072, 0.054, and 0.045 chains/nm^2 for PLys20, 42, and 69, respectively. Indeed, PEG density analysis clarified that CPMs of lower PLys DP retained higher PEG density and thereby likely contributed to lower cellular uptake efficiency.

3.4. Effect of rod length of PMs on their cellular uptake

In addition, there is another issue to be considered with regard to cellular uptake, because PLys DP modulation affects not only PEG density [17] but also rod length distribution [17,18]. CPMs of lower PLys DP exhibited a longer rod length distribution (Fig. 2d, Fig. S4d for representative TEM images), whereas those of higher PLys DP exhibited a shorter rod length distribution (Fig. 2f, Fig. S4f for

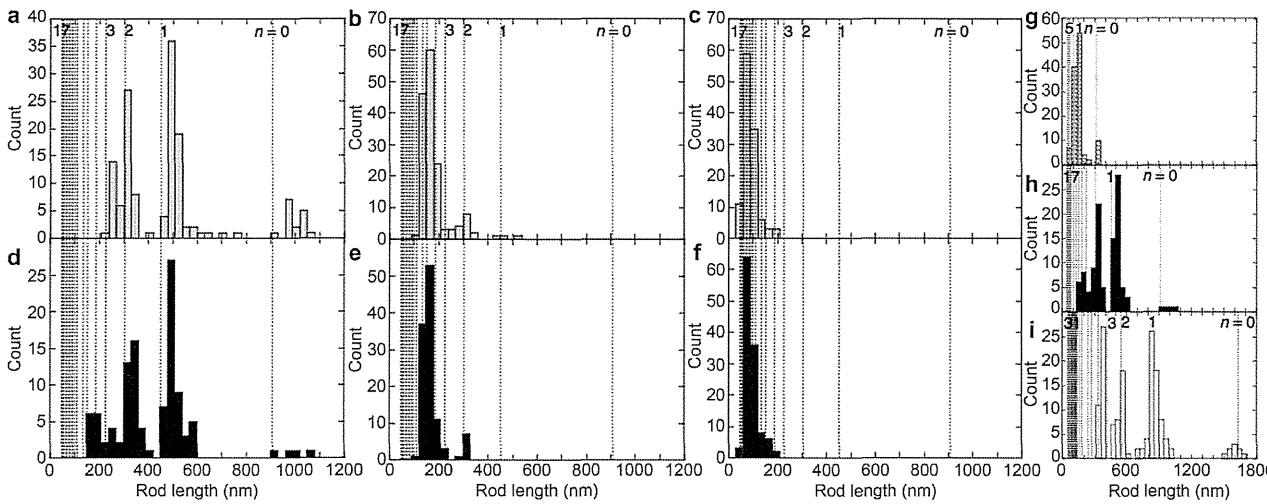

Fig. 2. Rod length distribution of PMs obtained by measuring the major axis length of the rod structures using TEM images. (a–c): Non-CPMs of pCAG–Luc2 (6477 bp); (a) PEG–PLys20, (b) PEG–PLys42, and (c) PEG–PLys69. (d–f): CPMs of pCAG–Luc2; (d) PEG–PLys20(SH), (e) PEG–PLys42(SH), and (f) PEG–PLys69(SH). (g–i): CPMs of differently sized pDNAs with fixed PEG–PLys20(SH); (g) pKF18 (2204 bp), (h) pCAG–Luc2 (6477 bp), and (i) pAUR316 (11,613 bp). Representative TEM images of (a–f) and (g–i) are shown in Figs. S4 and S5, respectively. Dotted vertical lines represent the theoretical rod lengths expected on the basis of the quantized folding scheme at each folding number (n).

representative TEM images). The longer rod length may also be a problem for efficient cellular uptake because it has been claimed that the process of each endocytosis has an upper size limit with regard to the diameter of the endocytic vesicles [38]. Because HeLa cells are generally considered to be nonphagocytic [39], the possibility of phagocytosis could be excluded. Then, the following four possible endocytic pathways should be considered: macropinocytosis and clathrin-dependent, caveolae-dependent, and clathrin/caveolae-independent endocytosis, with the upper size restriction of the endocytic vesicles being 5 μm [40], 200 nm [41,42], 80 nm [43], and 90 nm [38], respectively. With regard to the rod length distribution for CPMs of PEG–PLys20(SH) loading pCAG–Luc2 (Fig. 2d), most of the rod length fraction was found to be above 200 nm, leaving a very small fraction below 200 nm. Taking this observation into consideration, limited cellular uptake of CPMs of PEG–PLys20(SH) may be reasonable because most of the fraction has to rely on only macropinocytosis. On the other hand, CPMs of PEG–PLys69(SH) (Fig. 2f) presenting their entire fraction below 200 nm may be taken up through all four endocytic pathways. This analysis clearly pointed out that the rod length of PMs may also be accountable for determining cellular uptake behavior (Fig. 1b).

To gain further insight on structural parameters (PEG density and rod length) contributing to cellular uptake, CPMs with different rod length distribution but retaining comparable PEG density were prepared using fixed DP of PLys20 of PEG–PLys(SH) (which provided the highest PEG density among the series of PLys DP) and three different pDNAs with varying lengths (pKF18: 2204 bp, pCAG–Luc2: 6477 bp, and pAUR316: 11,613 bp). As evidenced by the rod length distribution (Fig. 2g–i, Fig. S5a–c for representative TEM images), CPMs prepared from different pDNAs showed different rod length distribution, and it was found that pKF18 DNA retained a shorter rod length distribution, with a major fraction being below 200 nm (Fig. 2g), whereas pAUR316 DNA retained longer rod length distribution, with the entire fraction being above 200 nm (Fig. 2i). The similar PEG density of these CPMs of differently sized pDNAs was suggested by the similar folding number pattern (Fig. S8) because the folding number determines the rod length in the quantized folding scheme of pDNA [18] (Table S3) and is a function of PEG density [17]. The cellular uptake efficiency of these CPMs (PEG–PLys20(SH)) showed substantial rod length dependence (Fig. 1c); shorter rod CPMs of pKF18 DNA (mostly below 200 nm) were more readily internalized into the cells, whereas longer rod CPMs of pAUR316 DNA (entirely above 200 nm) exhibited limited uptake. These observations on CPMs with comparable PEG density indicate that the rod length of PM obviously plays a crucial role in cellular uptake efficiency. It should be noted that PMs of a longer rod length were indeed capable of being taken up, as also reported for micrometer-sized rod-shaped filomicelles [44]; however, their efficiency was limited. Particularly interest was that the critical rod length was consistent with the well-documented restriction size of clathrin-dependent endocytic vesicles (200 nm) [41,42].

In order to further promote cellular uptake efficiency, use of specific ligand is an effective strategy [21–24]. We applied cRGD peptide ligands on a series of PMs and examined the cellular uptake on HeLa cells, characterized by the overexpression of cRGD-specific $\alpha_v\beta_3$ and $\alpha_v\beta_5$ integrin receptors [21]. The promoted cellular uptake was obtained for all series of CPMs regardless of PLys DP (Fig. 1d) and pDNA size (Fig. 1c), which confirmed the significance of the effect of cRGD conjugation to promote cellular uptake. However, CPMs of PEG–PLys21(SH) with cRGD (R–PEG–PLys21(SH)) remained lower cellular uptake than those of other PLys DP with cRGD (Fig. 1d). This observation confirmed that rod length is an important structural parameter that should be primarily considered to achieve high cellular uptake.

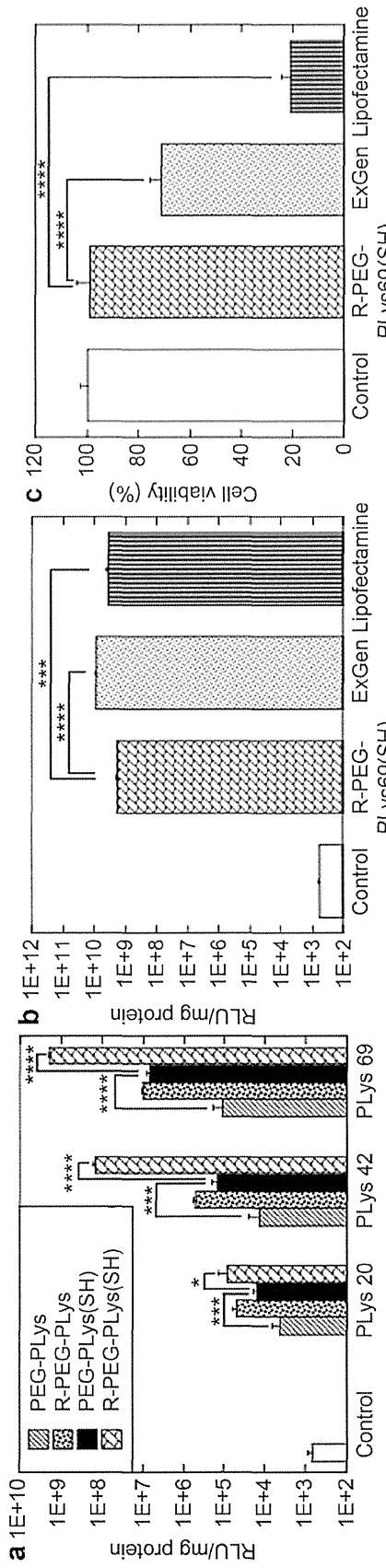

Fig. 3. Transfection efficiency and transfection-mediated cytotoxicity of PMs. (a) Transfection efficiency of both non-CPMs and CPMs of varying PLys DP with and without the cRGD ligand. Note that PLys20 in Fig. 3a represents either PEG–PLys20(SH) or R–PEG–PLys21(SH) and PLys42 represents either PEG–PLys42(SH) or R–PEG–PLys41(SH). (b) Transfection efficiency of R–PEG–PLys69(SH) compared with that of the commercial transfection reagents ExGen 500 and Lipofectamine® LTX with PLUS™. (c) Transfection-mediated cytotoxicity of R–PEG–PLys69(SH) compared with that of commercial reagents. Cells treated with HEPES were used as a control in all the experiments. pDNA encoding the luciferase gene (pCAG–Luc2) was used for all the experiments (mean ± SD, $n = 6$, two-tailed Student's *t*-test, $^*p < 0.05$, $^{***}p < 0.001$, $^{****}p < 0.0001$).

It would be interesting to examine whether rod length dependence is also applicable to other cell lines. Accordingly, we examined the cellular uptake efficiency of CPMs with and without the cRGD ligand using BxPC3 cells (epithelial cells) [45] (Fig. S9a) and human umbilical vein endothelial cells (HUVECs) [46] (endothelial cells) (Fig. S9b), both characterized by the overexpression of integrins binding to cRGD. We observed a quite consistent trend of PLys DP and cRGD effects, as observed in HeLa cells. Interestingly, CPMs of PEG–PLys20(SH) again exhibited substantially limited cellular uptake, validating the critical rod length for efficient cellular uptake and further demonstrating that the rod length of PMs should be regulated below 200 nm to induce efficient cellular uptake.

3.5. Transfection efficiency of PMs

Responding to the cellular uptake behavior, transfection efficiency was evaluated in HeLa cells using the reporter gene Luc (pCAG–Luc2 DNA). As shown in Fig. 3a, the trend of transfection efficiency appeared to be consistent with that of cellular uptake. PMs modified with cross-linking showed significantly higher gene expression efficiency than PMs without cross-linking. PMs with the cRGD ligand also exhibited higher gene expression efficiency than those without the cRGD ligand. Synergistically, PMs modified with both cross-linking and the cRGD ligand showed significantly augmented gene expression efficiency. Ultimately, with the rod length requirement of below 200 nm, cRGD-installed CPMs of PEG–PLys69(SH) [R–PEG–PLys69(SH)] exhibited the highest transfection efficiency among the other examined PMs. To evaluate the ability of R–PEG–PLys69(SH), the transfection efficiency was compared with that of well-acknowledged commercially available transfection reagents, cationic-polymer based ExGen 500 and cationic-lipid based Lipofectamine® LTX with PLUS™, at optimized preparations recommended by the manufacturer. Notably, the transfection efficiency of R–PEG–PLys69(SH) was almost comparable with that of the commercial transfection reagents (Fig. 3b) despite the fact that PM was covered with PEG palisade. Moreover, PMs do not possess any specific endosomal escape function such as the well-known proton sponge effect of ExGen 500 [47] and endosomolytic effect of Lipofectamine® LTX with PLUS™ [48]. In addition to the enhancement of cellular uptake by the use of the cRGD ligand, an alternative intracellular trafficking pathway to the nucleus should be involved because we observed that cRGD-installed PMs showed rapid accumulation in proximity to the nucleus [21,23], achieving such a high transfection efficiency. PMs also presented advantage with regard to cytotoxicity because the R–PEG–PLys69(SH) formulation did not show any transfection-mediated cytotoxicity, whereas ExGen 500 and Lipofectamine® LTX with PLUS™ showed a significant decrease in cell viability (Fig. 3c) evaluated at an equivalent dose used for the transfection study (1 μg of pDNA/well), further validating the high potency of this PM formulation in terms of the safety concern.

3.6. Systemic treatment of xenografted pancreatic tumors by PMs loaded with sFlt-1-encoding pDNA

Given the advanced functions of the R–PEG–PLys69(SH) formulation, including systemic application as a PEG palisade for providing stealth effect, core cross-linking for avoiding unfavorable disassembly in blood circulation, and a cRGD ligand as a tumor-targeting moiety, this formulation was challenged to treat pancreatic tumor, one of the most intractable solid tumors, in mice with subcutaneous xenografts of BxPC3 human pancreatic adenocarcinoma. It should be noted that BxPC3 xenografts are characterized by hypovascularity and reduced vascular permeability due to thick pericyte coverage around the tumor blood vessels [49,50]. In addition, the tumor nest is surrounded by a fibroblast-rich stromal matrix [49–52], thereby limiting the access of therapeutic agents to the tumor cells. With this regard, tumor vascular endothelial cells (VECs) were targeted by noting that VECs are featured by overexpression of $\alpha_v\beta_3$ and $\alpha_v\beta_5$ integrin receptors [53]. As a strategy for suppressing tumor growth, an antiangiogenic approach was chosen using a gene encoding a potent antiangiogenic exogenous protein, sFlt-1, which captures vascular endothelial growth factor (VEGF), exerting an antiangiogenic effect [54,55]. The therapeutic activity of PMs loading either pCAG–sFlt-1 or pCAG–Luc2 DNA (control), followed by intravenous injection, was evaluated by the tumor growth inhibition study. As presented in Fig. 4, compared with the control group, significant suppression of tumor growth was observed in the sFlt-1-treated group, thereby validating the feasibility of R–PEG–PLys69(SH) as a formulation for systemic gene therapy. To confirm that the obtained tumor growth inhibition was due to sFlt-1 protein expression at the tumor site, tumor cryosections were histologically analyzed and the level of sFlt-1 expression was quantified with an antibody that binds to sFlt-1 and inherently expressed VEGFR-1. The immunofluorescent-stained images showed remarkable sFlt-1 expression at the tumor site (Fig. 5c). Notably, most of the sFlt-1 protein was found in the region of the tumor stroma adjacent to VECs. Presumably, the secreted sFlt-1 protein from transfected cells captured VEGF and limited the binding to VEGFR-1, thereby preventing endothelial cell proliferation and consequently inhibiting neovasculature formation (antiangiogenesis). Indeed, the inhibition of neovascularization was confirmed by the reduced vascular density of tumor treated with sFlt-1 loaded R–PEG–PLys69(SH) in comparison with that of the control group (HEPES) (Fig. 5h), as shown by immunofluorescent staining of VECs using PECAM-1 (Fig. 5e,g). These evaluations confirmed that the obtained antitumor activity was certainly attributed to antiangiogenesis by the expressed sFlt-1 protein, which ultimately led to the suppression of tumor growth. Along with the immunofluorescent staining method, we previously confirmed that the sFlt-1 protein was specifically found at the tumor site and not in any other normal organs by enzyme-linked immunosorbent assay (ELISA) for the similar CPM system [15].

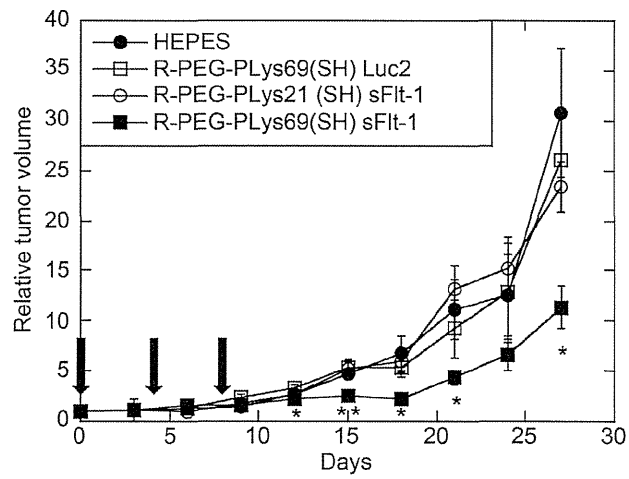

Fig. 4. Antitumor activity of cRGD-conjugated CPMs (R-CPMs) loading either pCAG–sFlt-1 or pCAG–Luc2 pDNA in subcutaneous BxPC3 tumor-bearing mice via intravenous administration. Mice injected with HEPES and CPMs of R–PEG–PLys69(SH) loading Luc2-expressing pDNA were used as control groups. R-CPMs were administered on days 0, 4, and 8 (indicated by arrows). Data points marked with asterisks show statistical significance for CPMs of R–PEG–PLys69(SH) loading sFlt-1-injecting group relative to not only control groups but also R–PEG–PLys21(SH) (mean ± SEM, $n = 4$, two-tailed Student's t-test, $^*p < 0.05$, $^{**}p < 0.01$).

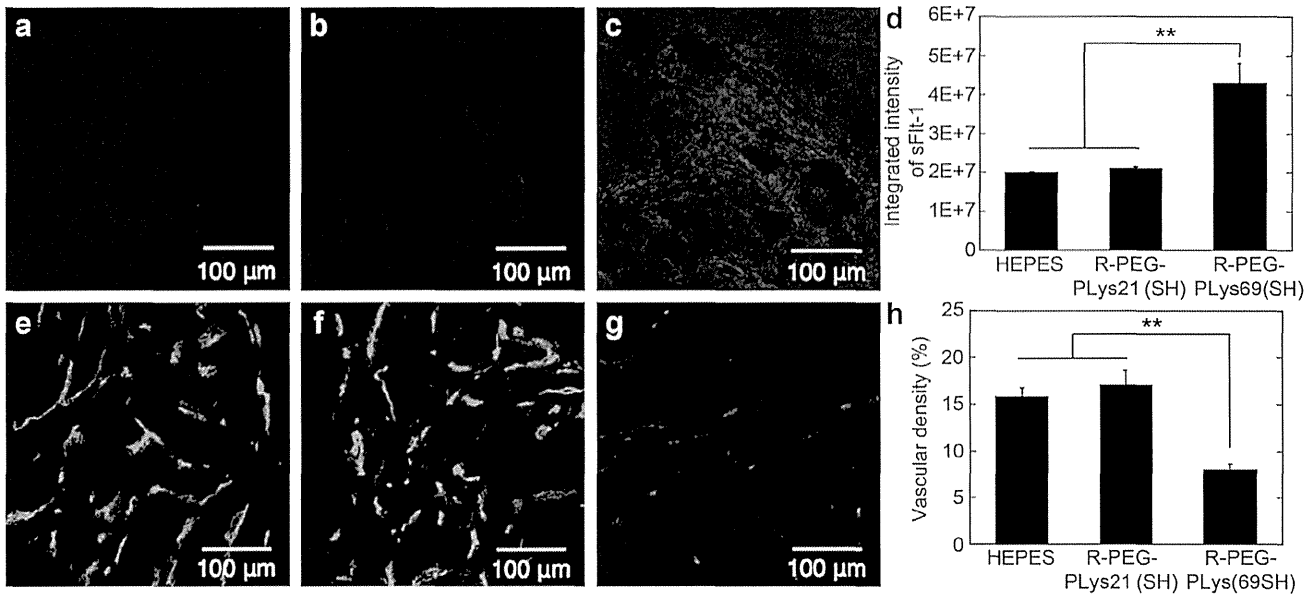

Fig. 5. Histological examination of BxPC3 tumor tissue after intravenous administration of R-CPMs containing sFlt-1 pDNA. Top row: Representative CLSM images of sFlt-1 protein expression in tumor cryosections of (a) HEPES (control), (b) R–PEG–PLys21(SH), and (c) R–PEG–PLys69(SH). Green: expressed sFlt-1 (or inherent VEGFR-1); red: vascular endothelial cells; blue: nucleus. (d) Integrated density of sFlt-1/VEGFR-1-positive fluorescence quantified from CLSM images (mean ± SD, $n = 6$, two-tailed Student's *t*-test, $^{**}p < 0.01$). Bottom row: Representative CLSM images of immunofluorescent-stained VECs (green) of the tumor vasculature using PECAM-1 in tumor cryosections of (e) HEPES (control), (f) R–PEG–PLys21(SH), (g) R–PEG–PLys69(SH), and (h) percentage area of PECAM-1-positive region quantified from CLSM images (mean ± SD, $n = 6$, two-tailed Student's *t*-test, $^{**}p < 0.01$).

Notably, CPMs of lower PLys DP exhibited higher PEG density, thus can be expected for better blood circulation. Accordingly, effective antitumor efficacy can be readily anticipated for R–PEG–PLys21(SH) because PMs have an increased chance of accumulating at the targeted tumor site. However, this formulation did not exhibit significant antitumor efficacy (Fig. 4), although PEG–PLys20(SH) exhibited a better blood retention time than PEG–PLys69(SH) (Fig. S10). Most likely, the inferior cellular uptake for CPMs of R–PEG–PLys21(SH) due to the longer rod length, as observed in the *in vitro* study (Fig. 1c), may result in limited transfection of the targeted cells. It should be noted that CPMs of PEG–PLys20(SH) loading pCAG–sFlt-1 DNA (7186 bp) exhibited most of the rod length fraction above 200 nm, while those of PEG–PLys69(SH) exhibited most of the rod length fraction below 200 nm (Fig. S11). Indeed, neither sFlt-1 expression (Fig. 5b) nor decreased vascular density (Fig. 5f) was observed for R–PEG–PLys21(SH) at the tumor site. This result validated the significance of regulating the rod length of PMs for promoting *in vivo* gene transfection upon systemic administration, concurrently encouraging subsequent research to develop an ideal systemic gene delivery system with prolonged blood circulation capacity on the basis of this recognized PM formulation.

4. Conclusions

Aiming to capture the correlation between structural features of PMs and biological performance, we intensively studied the effect of PLys DP on cellular uptake, integrating previously approved strategies such as disulfide cross-linking and use of the cRGD moiety as a ligand for improving cellular uptake efficiency. The structural features of PMs such as stability of assembly and PEG density affected cellular uptake efficiency; however, rod length was found to be the most significant parameter affecting cellular uptake. With a critical rod length of 200 nm, which is consistent with the well-documented upper size limit of clathrin-dependent endocytic vesicles, PMs with a longer rod showed limited uptake, whereas those with a shorter rod showed efficient uptake. In particular, coupling with cross-linking and the cRGD ligand substantially elevated the cellular uptake. Consequently, the PM formulation satisfying all these parameters, i.e., R–PEG–PLys69(SH), showed promoted transfection efficiency almost comparable with that of ExGen 500 and Lipofectamine® LTX with PLUS™, well-known transfection reagents, despite the fact that PMs did not have any specific endosomal escape function and were also covered by PEG. Upon systemic administration, the identified R–PEG–PLys69(SH), with advanced features for systemic tumor therapy by virtue of PEG shielding, core cross-linking, and the cRGD ligand, exhibited significant antitumor efficacy against a stroma-rich pancreatic tumor model through an antiangiogenic effect. Furthermore, CPMs of R–PEG–PLys21(SH) with most of the rod length fraction above 200 nm resulted in no significant antitumor efficacy even if this formulation showed a better blood retention profile than PLys69, approving a critical role of rod length even in *in vivo* gene transfection. Therefore, the present study clearly identified the importance of regulating the length of rod-shaped PMs to obtain efficient gene transfection not only in cultured cell lines but also in systemic applications.

Acknowledgments

This work was financially supported by the Core Research Program for Evolutional Science and Technology (CREST) and Precursory Research for Embryonic Science and Technology (PRESTO) from the Japan Science and Technology Corporation (JST), and by the Japan Society for the Promotion of Science (JSPS) through its Funding Program for World-Leading Innovative R&D on Science and Technology (FIRST Program), Grant-in-Aid for Specially promoted Research, and Core to Core Program for A. Advanced Research Networks. The authors thank Dr. S. Fukuda from the University of Tokyo Hospital for his valuable assistance in conducting TEM and Mr. H. Hoshi from JEOL Ltd. for his valuable assistance in conducting cryo-TEM observation in Research Hub for

Advanced Nano Characterization, The University of Tokyo, supported by the Ministry of Education, Culture, Sports, Science, and Technology (MEXT) of Japan. A.D. acknowledges the fellowship from MEXT.

Appendix A. Supplementary data

Supplementary data related to this article can be found at http://dx.doi.org/10.1016/j.biomaterials.2014.03.037.

References

[1] Kabanov AV. Polymer genomics: an insight into pharmacology and toxicology of nanomedicines. Adv Drug Deliv Rev 2006;58:1597–621.
[2] Cabral H, Nishiyama N, Kataoka K. Supramolecular nanodevices: from design validation to theranostic nanomedicine. Acc Chem Res 2011;44:999–1008.
[3] Hubbell JA, Chilkoti A. Nanomaterials for drug delivery. Science 2012;37:303–5.
[4] Kopecek J. Polymer-drug conjugates: origins, progress to date and future directions. Adv Drug Deliv Rev 2013;65:49–59.
[5] Mulligan RC. The basic science of gene therapy. Science 1993;260:926–32.
[6] Kay MA. State-of-the-art gene-based therapies: the road ahead. Nat Rev Genet 2011;12:316–28.
[7] Osada K, Christie JR, Kataoka K. Polymeric micelles from poly(ethylene glycol)-poly(amino acid) block copolymer for drug and gene delivery. J R Soc Interface 2009;6:S325–39.
[8] Miyata K, Nishiyama N, Kataoka K. Rational design of smart supramolecular assemblies for gene delivery: chemical challenges in the creation of artificial viruses. Chem Soc Rev 2012;41:2562–74.
[9] Ogris M, Brunner S, Schuller S, Kircheis R, Wagner E. PEGylated DNA/transferrin–PEI complexes: reduced interaction with blood components, extended circulation in blood and potential for systemic gene delivery. Gene Ther 1999;4:595–605.
[10] Katayose S, Kataoka K. Water-soluble polyion complex associates of DNA and poly(ethylene glycol)-poly(L-lysine) block copolymer. Bioconjug Chem 1997;8:702–7.
[11] Kakizawa Y, Kataoka K. Block copolymer micelles for delivery of gene and related compounds. Adv Drug Deliv Rev 2002;54:203–22.
[12] Osada K, Oshima H, Kobayashi D, Doi M, Enoki M, Yamasaki Y, et al. Quantized folding of plasmid DNA condensed with block catiomer into characteristic rod structures promoting transgene efficacy. J Am Chem Soc 2010;132:12343–8.
[13] Akagi D, Oba M, Koyama H, Nishiyama N, Fukushima S, Miyata T, et al. Biocompatible micellar nanovectors achieve efficient gene transfer to vascular lesions without cytotoxicity and thrombus formation. Gene Ther 2007;14:1029–38.
[14] Miyata K, Kakizawa Y, Nishiyama N, Harada A, Yamasaki Y, Koyama H, et al. Block catiomer polyplexes with regulated densities of charge and disulfide cross-linking directed to enhance gene expression. J Am Chem Soc 2004;126:2355–61.
[15] Oba M, Vachutinsky Y, Miyata K, Kano MR, Ikeda S, Nishiyama N, et al. Antiangiogenic gene therapy of solid tumor by systemic injection of polyplex micelles loading plasmid DNA encoding soluble Flt-1. Mol Pharm 2010;7:501–9.
[16] Vachutinsky Y, Oba M, Miyata K, Hiki S, Kano MR, Nishiyama N, et al. Antiangiogenic gene therapy of experimental pancreatic tumor by sFlt-1 plasmid DNA carried by RGD-modified crosslinked polyplex micelles. J Control Release 2011;149:51–7.
[17] Tockary TA, Osada K, Chen Q, Machitani K, Dirisala A, Uchida S, et al. Tethered PEG crowdedness determining shape and blood circulation profile of polyplex micelle gene carriers. Macromolecules 2013;46:6585–92.
[18] Osada K, Shiotani T, Tockary TA, Kobayashi D, Oshima H, Ikeda S, et al. Enhanced gene expression promoted by the quantized folding of pDNA within polyplex micelles. Biomaterials 2012;33:325–32.
[19] Lu F, Wu SH, Hung Y, Mou CY. Size effect on cell uptake in well-suspended, uniform mesoporous silica nanoparticles. Small 2009;5:1408–13.
[20] Katayose S, Kataoka K. Remarkable increase in nuclease resistance of plasmid DNA through supramolecular assembly with poly(ethylene glycol)–poly(L-lysine)block copolymer. J Pharm Sci 1998;87:160–3.
[21] Oba M, Fukushima S, Kanayama N, Aoyagi K, Nishiyama N, Koyama H, et al. Cyclic RGD peptide-conjugated polyplex micelles as a targetable gene delivery system directed to cells possessing $\alpha_v\beta_3$ and $\alpha_v\beta_5$ integrins. Bioconjug Chem 2007;18:1415–23.
[22] Oba M, Aoyagi K, Miyata K, Matsumoto Y, Itaka K, Nishiyama N, et al. Polyplex micelles with cyclic RGD peptide ligands and disulfide cross-links directing to the enhanced transfection via controlled intracellular trafficking. Mol Pharm 2008;5:1080–92.
[23] Mickler FM, Vachutinsky Y, Oba M, Miyata K, Nishiyama N, Kataoka K, et al. Effect of integrin targeting and PEG shielding on polyplex micelle internalization studied by live-cell imaging. J Control Release 2011;156:364–73.
[24] Ge Z, Chen Q, Osada K, Liu X, Tockary TA, Uchida S, et al. Targeted gene delivery by polyplex micelles with crowded PEG palisade and cRGD moiety for systemic treatment of pancreatic tumors. Biomaterials 2014;35:3416–26.
[25] Daly WH, Poché D. The preparation of *N*-carboxyanhydrides of α-amino acids using bis(trichloromethyl)carbonate. Tetrahedron Lett 1998;29:5859–62.
[26] Tam JP, Wu CR, Liu W, Zhang JW. Disulfide bond formation in peptides by dimethyl sulfoxide. Scope and applications. J Am Chem Soc 1991;113:6657–62.
[27] Itaka K, Yamauchi K, Harada A, Nakamura K, Kawaguchi H, Kataoka K. Polyion complex micelles from plasmid DNA and poly(ethylene glycol)-poly(L-lysine) block copolymer as serum-tolerable polyplex system: physicochemical properties of micelles relevant to gene transfection efficiency. Biomaterials 2003;24:4495–506.
[28] von Köckritz-Blickwede M, Chow OA, Nizet V. Fetal calf serum contains heat-stable nucleases that degrade neutrophil extracellular traps. Blood 2009;114:5245–6.
[29] Bernfield M, Götte M, Park P. Functions of cell surface heparan sulfate proteoglycans. Annu Rev Biochem 1999;68:729–77.
[30] Tumova S, Woods A, Couchman JR. Heparan sulfate proteoglycans on the cell surface: versatile coordinators of cellular functions. Int J Biochem Cell Biol 2000;32:269–88.
[31] Burke RS, Pun SH. Extracellular barriers to *in vivo* PEI and PEGylated PEI polyplex-mediated gene delivery to the liver. Bioconjug Chem 2008;19:693–704.
[32] Ruponen M, Ylä-Herttuala S, Urtti A. Interactions of polymeric and liposomal gene delivery systems with extracellular glycosaminoglycans: physicochemical and transfection studies. Biochim Biophys Acta 1999;1415:331–41.
[33] Yanagishita M, Hascall VC. Characterization of heparan sulfate proteoglycans synthesized by rat ovarian granulosa cells in culture. J Biol Chem 1983;8:12857–64.
[34] Pikas DS, Li J-P, Vlodavsky I, Lindahl U. Substrate specificity of heparanases from human hepatoma and platelets. J Biol Chem 1998;273:18770–7.
[35] Kakizawa Y, Harada A, Kataoka K. Environment-sensitive stabilization of core-shell structured polyion complex micelle by reversible cross-linking of the core through disulfide bond. J Am Chem Soc 1999;121:11247–8.
[36] Kursa M, Walker GF, Roessler V, Ogris M, Roedl W, Kircheis R, et al. Novel shielded transferrin-polyethylene glycol-polyethylenimine/DNA complexes for systemic tumor-targeted gene transfer. Bioconjug Chem 2003;14:222–31.
[37] Mishra S, Webster P, Davis ME. PEGylation significantly affects cellular uptake and intracellular trafficking of non-viral gene delivery particles. Eur J Cell Biol 2004;83:97–111.
[38] Conner SD, Schimd SL. Regulated portals of entry into the cell. Nature 2003;422:37–44.
[39] Kobayahi M, Hoshino T. Phagocytic activity of HeLa cells after thymidine treatment. Arch Histol Jpn 1983;46:479–89.
[40] Lim JP, Gleeson PA. Macropinocytosis: an endocytic pathway for internalising large gulps. Immunol Cell Biol 2011;89:836–43.
[41] McMahon HT, Boucrot E. Molecular mechanism and physiological functions of clathrin-mediated endocytosis. Nat Rev Mol Cell Biol 2011;12:517–33.
[42] Rejman J, Oberle V, Zuhorn IS, Hoekstra D. Size-dependent internalization of particles via the pathways of clathrin- and caveolae-mediated endocytosis. Biochem J 2004;377:159–69.
[43] Pelkmans L, Helenius A. Endocytosis via caveolae. Traffic 2002;3:311–20.
[44] Geng Y, Dalhaimer P, Cai SS, Tsai R, Tewari M, Minko T, et al. Shape effects of filaments versus spherical particles in flow and drug delivery. Nat Nanotechnol 2007;2:249–55.
[45] Ji S, Xu J, Zhang B, Yao W, Xu W, Wu W, et al. RGD-conjugated albumin nanoparticles as a novel delivery vehicle in pancreatic cancer therapy. Cancer Biol Ther 2012;13:206–15.
[46] Kagaya H, Oba M, Miura Y, Koyama H, Ishii T, Shimada T, et al. Impact of polyplex micelles installed with cyclic RGD peptide as ligand on gene delivery to vascular lesions. Gene Ther 2012;19:61–9.
[47] Boussif O, Lezoualch F, Zanta MA, Mergny MD, Scherman D, Demeneix B, et al. A versatile vector for gene and oligonucleotide transfer into cells in culture and *in vivo*: polyethylenimine. Proc Natl Acad Sci U S A 1995;92:7297–301.
[48] Zhou X, Huang L. DNA transfection mediated by cationic liposomes containing lipopolylysine: characterization and mechanism of action. Biochim Biophys Acta 1994;1189:195–203.
[49] Kano MR, Komuta Y, Iwata C, Oka M, Shirai Y, Morishita Y, et al. Comparison of the effects of the kinase inhibitors imatinib, sorafenib, and transforming growth factor-beta receptor inhibitor on extravasation of nanoparticles from neovasculature. Cancer Sci 2009;100:173–80.
[50] Kano MR, Bae Y, Iwata C, Morishita Y, Yashiro M, Oka M, et al. Improvement of cancer-targeting therapy, using nanocarriers for intractable solid tumors by inhibition of TGF-beta signaling. Proc Natl Acad Sci U S A 2007;104:3460–5.
[51] Sofuni A, Iijima H, Moriyasu F, Nakayama D, Shimizu M, Nakamura K, et al. Differential diagnosis of pancreatic tumors using ultrasound contrast imaging. J Gastroenterol 2005;40:518–25.
[52] Takahashi Y, Cleary KR, Mai M, Kitadai Y, Bucana CD, Ellis LM. Significance of vessel count and vascular endothelial growth factor and its receptor (KDR) in intestinal-type gastric cancer. Clin Cancer Res 1996;2:1679–84.
[53] Erdreich-Epstein A, Shimada H, Groshen S, Liu M, Metelitsa LS, Kim KS, et al. Integrins $\alpha_v\beta_3$ and $\alpha_v\beta_5$ are expressed by endothelium of high-risk neuroblastoma and their inhibition is associated with increased endogenous ceramide. Cancer Res 2000;60:712–21.
[54] Kendall RL, Thomas KA. Inhibition of vascular endothelial cell growth factor activity by an endogenously encoded soluble receptor. Proc Natl Acad Sci U S A 1993;90:10705–9.
[55] Yamaguchi S, Iwata K, Shibuya M. Soluble Flt-1 (soluble VEGFR-1), a potent natural antiangiogenic molecule in mammals, is phylogenetically conserved in avians. Biochem Biophys Res Commun 2002;291:554–9.

Journal of Controlled Release 183 (2014) 27–34

Contents lists available at ScienceDirect

Journal of Controlled Release

journal homepage: www.elsevier.com/locate/jconrel

Muscle-targeted hydrodynamic gene introduction of insulin-like growth factor-1 using polyplex nanomicelle to treat peripheral nerve injury

Kazuya Nagata [a], Keiji Itaka [a,*], Miyuki Baba [a], Satoshi Uchida [a], Takehiko Ishii [b], Kazunori Kataoka [a,c,**]

[a] Division of Clinical Biotechnology, Center for Disease Biology and Integrative Medicine, Graduate School of Medicine, The University of Tokyo, Japan
[b] Department of Bioengineering, Graduate School of Engineering, The University of Tokyo, Japan
[c] Department of Materials Engineering, Graduate School of Engineering, The University of Tokyo, Japan

ARTICLE INFO

Article history:
Received 30 August 2013
Accepted 10 March 2014
Available online 20 March 2014

Keywords:
Peripheral nerve injury
Muscle atrophy
Insulin-like growth factor-1 (IGF-1)
Gene delivery
Hydrodynamic injection
Polyplex nanomicelle

ABSTRACT

The recovery of neurologic function after peripheral nerve injury often remains incomplete because of the prolonged reinnervation process, which leads to skeletal muscle atrophy and articular contracture from disuse over time. To rescue the skeletal muscle and promote functional recovery, insulin-like growth factor-1 (IGF-1), a potent myogenic factor, was introduced into the muscle by hydrodynamic injection of IGF-1-expressing plasmid DNA using a biocompatible nonviral gene carrier, a polyplex nanomicelle. In a mouse model of sciatic nerve injury, the introduction of IGF-1 into the skeletal muscle of the paralyzed limb effectively alleviated a decrease in muscle weight compared with that in untreated control mice. Histologic analysis of the muscle revealed the IGF-1-expressing plasmid DNA (pDNA) to have a myogenic effect, inducing muscle hypertrophy with the upregulation of the myogenic regulatory factors, myogenin and MyoD. The evaluation of motor function by walking track analysis revealed that the group that received the hydrodynamic injection of IGF-1-expressing pDNA using the polyplex nanomicelle had significantly early recovery of motor function compared with groups receiving negative control pDNA and untreated controls. Early recovery of sensation in the distal area of sciatic nerve injury was also induced by the introduction of IGF-1-expressing pDNA, presumably because of the effect of secreted IGF-1 protein in the vicinity of the injured sciatic nerve exerting a synergistic effect with muscle hypertrophy, inducing a more favorable prognosis. This approach of introducing IGF-1 into skeletal muscle is promising for the treatment of peripheral nerve injury by promoting early motor function recovery.

1. Introduction

The recovery of neurologic function after peripheral nerve injury is often incomplete because of the prolonged reinnervation process. A variety of approaches directed at enhancing nerve regeneration has been investigated using nerve growth factors such as fibroblast growth factor-2 (FGF-2) [1], glial cell line-derived neurotrophic factor (GDNF) [2,3], brain-derived neurotrophic factor (BDNF) [4], and vascular endothelial growth factor (VEGF) [5,6]. However, the inherently limited rate of axonal regrowth leads to muscle atrophy and articular contracture because of disuse over time, hampering the full recovery of motor function despite physical therapy and additional treatments.

Insulin-like growth factor-1 (IGF-1) is a potent myogenic factor. Several basic studies using transgenic mice overexpressing IGF-1 have revealed that IGF-1 promotes muscle regeneration by regulating myoblast proliferation, myogenic differentiation, and myotube hypertrophy [7–10]. Thus, administration of IGF-1 has potential as a treatment to rescue muscles affected by disuse atrophy, thereby promoting functional recovery after injury.

Therefore, the introduction of a gene expressing IGF-1 is believed to be an effective treatment strategy. Although several approaches using IGF-1 recombinant protein or its fusion either by systemic injection or intramuscular injection showed efficacy for the induction of muscle hypertrophy [11–13], the use of gene introduction has advantages in providing higher and sustained IGF-1 expression in skeletal muscle [14]. Various trials of IGF-1 gene administration using naked plasmid DNA (pDNA) with electroporation or an adeno-associated virus vector showed an effect on inducing muscle hypertrophy in animal models of muscle disuse or myotoxic injury [15–19]. However, with regard to clinical availability, there still are problems associated with gene introduction, such as the highly invasive manner of electroporation and risks

* Correspondence to: K. Itaka, Division of Clinical Biotechnology, Center for Disease Biology and Integrative Medicine, Graduate School of Medicine, The University of Tokyo, 7-3-1 Hongo, Bunkyo-ku, Tokyo 113-0033, Japan. Tel.: +81 3 5841 1418; fax: +81 3 5841 1419.
** Correspondence to: K. Kataoka, Department of Materials Engineering, Graduate School of Engineering, The University of Tokyo, 7-3-1 Hongo, Bunkyo-ku, Tokyo 113-0033, Japan. Tel.: +81 3 5841 7138; fax: +81 3 5841 7139.
E-mail addresses: itaka-ort@umin.net (K. Itaka), kataoka@bmw.t.u-tokyo.ac.jp (K. Kataoka).

http://dx.doi.org/10.1016/j.jconrel.2014.03.021
0168-3659/

of natural viruses. Moreover, although the effect of IGF-1 on muscle fibers has been intensely studied by histologic and molecular biologic analyses, the final outcome on the recovery of motor function remains unclear.

In this study, we proposed a novel approach to introduce IGF-1-expressing pDNA with high efficacy and minimal tissue damage to the muscle, hydrodynamic injection of polyplex nanomicelle into the skeletal muscle. Hydrodynamic injection is a promising approach to enhance transgene expression due to the transient increase in hydrostatic pressure in the target tissue and organ [20,21]. For targeting skeletal muscle, we previously reported that our original nonviral gene carrier, polyplex nanomicelle, effectively provided high transgene expression following hydrodynamic injection into a distal vein with isolation of the limb by tourniquet [22,23].

The polyplex nanomicelle is a nonviral carrier composed of pDNA and poly(ethyleneglycol) (PEG)-block-polycation, forming a micelle structure with a diameter of several-tens nm surrounded by a hydrophilic and electrically neutral palisade of PEG [23,24]. This structure increases the steric stability of polyplexes under physiological conditions and exhibits less nonspecific interaction with biologic components such as serum proteins. In addition, our original polycation, poly{N′-[N-(2-aminoethyl)-2-aminoethyl]aspartamide} [PAsp(DET)], used as a core-forming segment of polyplex nanomicelles, was developed to increase transfection efficiency with minimal cytotoxicity due to its self-catalytic degradability under physiological conditions [25,26]. Using this system, we have already achieved therapeutic effects including bone regeneration in critical bony defects of mice by introducing osteogenic transcription factors [27] and regulation of right heart pressure in a mouse model of idiopathic pulmonary hypertension by introducing adrenomedullin [28].

Based on the properties described, the nanomicelle is beneficial to increase cellular uptake and subsequent high transgene expression in skeletal muscle compared with the hydrodynamic injection of naked pDNA [22]. Moreover, the nanomicelle allows uniformly-distributed transgene expression in the muscle fibers, presumably due to the well-regulated particle size of several-tens nm that improves tissue penetration upon injection. In addition, the combined use of an anionic polysaccharide, chondroitin sulfate (CS), significantly reduced the tissue damage and inflammatory responses in skeletal muscle after the hydrodynamic injection, leading to prolonged transgene expression for more than a month [29].

We applied this method to introduce IGF-1-expressing pDNA into the skeletal muscle to treat mice with sciatic nerve injury. The effect of IGF-1 on muscle hypertrophy and the resulting therapeutic effect on motor function were thoroughly investigated, including a behavioral analysis of mice. Based on the outcomes, the applicability of this system for the treatment of peripheral nerve injury is discussed in detail.

2. Materials and methods

2.1. Materials

Plasmid DNAs (pDNAs) encoding IGF-1 and β-galactosidase (β-gal) were purchased from InvivoGen (pBLAST44-mIGF-1a; San Diego, CA, USA) and Promega (pSV-β-galactosidase; Madison, WI, USA), respectively. The pDNA concentration was determined by reading the absorbance at 260 nm. Chondroitin sulfate A (CS) and streptozotocin were purchased from Sigma Aldrich (St Louis, MO, USA).

2.2. Animals

Balb/c albino mice (female; 10 14 weeks old) were purchased from Charles River Laboratories (Tokyo, Japan). All animal experimental protocols were performed in accordance with the approval of the Animal Care and Use Committee of the University of Tokyo.

2.3. Preparation of polyplex nanomicelles in combination with CS

For hydrodynamic introduction of pDNA into skeletal muscle, a system of polyplex nanomicelles based on a block copolymer of PEG and poly{N′-[N-(2-aminoethyl)-2-aminoethyl]aspartamide} [PEG-PAsp(DET)] was used. This block copolymer was synthesized as previously reported [25]. The molecular weight of PEG was 12,000, and the polymerization degree of the PAsp(DET) segment was determined to be 69 by ^{1}H-NMR. The block copolymer and pDNA were separately dissolved in 10 mM Tris–HCl buffer (pH 7.4). PEG-PAsp(DET)/pDNA polyplex nanomicelles were obtained by simply mixing both solutions.

Before hydrodynamic injection, CS solution was added to the nanomicelle solution because we had observed that CS had remarkable effects on a reduction in tissue damage and prolonged transgene expression after hydrodynamic injection into skeletal muscle [29]. Based on the study, the mixing ratio of amino groups in PEG-PAsp(DET), phosphate groups in pDNA, and the total carboxyl and sulfate groups in CS was set to 20:1:100 as the optimal condition to obtain efficient transgene expression. The final concentration of pDNA was adjusted to 134 μg/mL. Immediately before injection into mice, a 1/100 volume of 5 M NaCl solution was added to form a half-isotonic solution.

2.4. Hydrodynamic injection into the limb vein of mice

Hydrodynamic gene introduction into skeletal muscle was performed as previously reported [22]. In brief, after anesthetizing mice with 3% isoflurane (Abbott Japan Co., Ltd., Tokyo, Japan), a tourniquet was placed on the proximal thigh to transiently restrict blood flow. From a distal site of the great saphenous vein, the nanomicelle solution or naked pDNA (375 μL; containing 50 μg pDNA) was injected over 5 s. At 5 min after the injection, the tourniquet was released. For negative controls, the same volume of physiological saline was injected using the same procedure.

2.5. Intramuscular injection into the limb

The nanomicelle solution or naked pDNA was prepared similarly as the case for hydrodynamic injection at greater concentration of pDNA (50 μL; containing 50 μg pDNA). The injection was done at the center of muscle belly of quadriceps femoris.

2.6. Surgical procedure to create sciatic nerve injury

One hour after the hydrodynamic injection, a surgical procedure was performed to create a cryo-injury of the sciatic nerve [30]. A skin incision was made at the right greater trochanter, and the right sciatic nerve was carefully exposed without damaging the muscle. At a point immediately distal to the gluteus maximus muscle, the nerve was grasped for 30 s using hemostatic forceps, which had been chilled in advance with liquid nitrogen for 30 s. This procedure was performed twice.

2.7. Real-time polymerase chain reaction (PCR)

To evaluate the IGF-1, MyoD and myogenin gene expression levels in the muscle, the mRNA expression levels were evaluated using real-time PCR. Seven days after the hydrodynamic injection, the mice were euthanized and the muscle of quadriceps femoris and triceps surae resected. The mRNA was purified from the muscle samples using RNeasy Fibrous Tissue Mini Kits (50) (Qiagen, Hilden, Germany). After reverse transcription using a QuantiTect Reverse Transcription Kit (Qiagen), real-time PCR was performed with QuantiTect SYBR Green PCR Master Mix (Qiagen) using an ABI Prism 7500 Sequence Detector (Applied Biosystems, Foster City, CA, USA). All expression data were normalized to the mRNA levels of β-actin. The primer sequences used were: IGF-1, forward primer TGGATGCTCTTCAGTTCGTG, reverse primer

GTCTTGGGCATGTCAGTGTG; β-actin, forward primer AGATGTGGATCA GCAAGCAG, reverse primer GCGCAAGTTAGGTTTTGTTCA. For myoD and myogenin, Taqman® gene expression assays were used (MyoD: Mm01203489_g1, myogenin: Mm00446195_g1). The ΔΔCt method was used to calculate the relative expression ratio.

2.8. Evaluation of muscle atrophy

The muscle weight was evaluated 7 days after injection by resecting the whole triceps surae mass from its origin at the popliteal fossa to insertion at the Achilles' tendon.

For histological analyses of the muscle to evaluate the muscle fiber hypertrophy, we obtained semi-thin fresh-frozen sections 7 or 16 days after the injection by a method using adhesive film (Cryofilm type IIC9, Section-lab, Hiroshima, Japan) [31,32]. This method allows for the preparation of sections from tissue samples containing calcified bone. In brief, mice were euthanized, and the limbs were resected and frozen in cooled isopentane. The frozen limbs were subsequently embedded in SCEM compound (Section-lab, Hiroshima, Japan). After the cut surface was covered with an adhesive film, frozen sections (for quadriceps femoris: 10-μm thick, 10-mm proximal from upper edge of patella, for triceps surae: 10-μm thick, 10-mm proximal from the heel) were obtained using a CM 3050S cryostat (Leica Microsystems, Wetzlar, Germany). The sections were stained with hematoxylin and eosin, and cross-sectional areas of individual muscle fibers were analyzed using image analysis software, ImageJ.

2.9. Walking track analysis

For the evaluation of motor function recovery, walking track analysis was performed [33]. Paw prints of the mice were recorded by moistening the hind paws of each animal with black ink and having them walk a 4.5 × 35-cm corridor in a darkroom. The tracks were evaluated for two different parameters: toe spread (TS), the distance between the first and fifth toes, and print length (PL), the distance between the third toe and the hind pad. The sciatic functional index (SFI) was calculated using the following formula:

$$SFI = 118.9 \times (ETS\text{-}NTS)/NTS\text{-}51.2 \times (EPL\text{-}NPL)/NPL\text{-}7.5$$

where EPL and ETS were the experimental print length and experimental toe spread, respectively, taken from the right paw, which received the sciatic nerve injury, and NPL and NTS were the normal print length and normal toe spread, respectively, taken from the normal left paw. In a preliminary experiment, normal mice without sciatic nerve injury had SFI values on the average of -12.4 ± 4.8 ($n = 4$); therefore, we set the normal range as > -15 in this experiment.

2.10. Preparation of mice diabetic model

To induce diabetes, a single intraperitoneal injection of streptozotocin (200 mg/kg body weight) was administrated to the mice [34]. Blood glucose levels were measured using Fuji DRI-CHEM slide GLU-WIII and DRI-CHEM 7000i (Fujifilm, Tokyo, Japan) seven days after the injection of streptozotocin. The mice exhibiting blood glucose levels >300 mg/dL served as diabetic animals for subsequent experiments.

2.11. Analyses of sensation

To evaluate the sensation in the paw after sciatic nerve injury, we performed two individual tests following procedures previously established. Constant pressure was applied to the soles of the feet with a clip. Paw withdrawal latencies were measured as an indication of sensitivity to pain [35]. To avoid overstimulation, each experiment was limited to 30 s.

In addition, we analyzed the response to cold [36]. After dipping the impaired hind paw into acetone, mice were immediately moved to a plastic cage, and the number of brisk foot withdrawal responses to the sensation of cold induced by evaporation of the acetone was measured.

2.12. Statistical analysis

Statistical analyses were done using one-way factorial analysis of variance (ANOVA) followed by the post hoc Tukey–Kramer correction for multiple comparisons. In all statistical analyses, significance was defined as $P < 0.05$.

3. Results

3.1. Effect of IGF-1-expressing pDNA to alleviate muscle atrophy after sciatic nerve injury

The IGF-1 expression levels in the quadriceps femoris and triceps surae were evaluated seven days after hydrodynamic injection of IGF-1-expressing pDNA using real-time PCR. The surgical treatment to induce sciatic nerve injury was performed to coincide with the injection of pDNA. In mice that received polyplex nanomicelles, the expression level of IGF-1 in the muscle was 37 times higher in quadriceps femoris and four times higher in triceps surae than those in untreated control mice (Fig. 1A, C). Injection of the identical amount of naked pDNA also showed an increase in IGF-1 expression; however, the level was lower than that identified in mice that received the nanomicelle. The myogenic regulatory factors myogenin and MyoD, known to be key molecules regulating muscle differentiation, showed upregulation in response to the introduction of IGF-1-expressing pDNA compared with saline controls and untreated controls. For quadriceps femoris, the group receiving nanomicelle induced significantly greater upregulation of myogenin and MyoD compared with naked pDNA, although there were no differences between the two groups receiving pDNA by nanomicelle or naked pDNA for triceps surae (Fig. 1B, D).

To evaluate the effects of IGF-1-expressing pDNA as a potent myogenic factor, the whole muscle weight was examined after resection of bilateral triceps surae seven days after sciatic nerve injury and concomitant hydrodynamic injection to the right leg. Compared with the normal opposite side (left) leg, the muscle weight of the right leg decreased to 65% in mice that received a hydrodynamic injection of saline and untreated control mice. The decrease for the mice receiving a hydrodynamic injection of naked IGF-1-expressing pDNA was alleviated to 68% to the normal leg, and to 81% for the mice that received a hydrodynamic injection of polyplex nanomicelle containing pDNA (Fig. 2). It is noted that the weight of the normal left leg showed small difference (~10%) among the four groups, however, there were no significant differences among the values. Although the reason for the difference in the muscle weight of the left leg remains unclear, it is confirmed that IGF-1-expressing pDNA showed a therapeutic effect to alleviate muscle weight decrease of the right leg induced by sciatic nerve injury. (Fig. 2).

3.2. IGF-1-expressing pDNA induced hypertrophy of muscle fibers

To directly evaluate the effect of IGF-1 on muscle fibers, we performed histologic analysis of the muscle after hydrodynamic injection of IGF-1-expressing pDNA. Cross-sections of quadriceps femoris were obtained 7 days after the injection to determine the average cross-sectional areas of individual muscle fibers. As shown in Fig. 3A–B, the group receiving nanomicelle showed significantly larger area of muscle fibers compared with other groups of receiving IGF-1-expressing pDNA (naked pDNA), β-gal-expressing pDNA (nanomicelle or naked pDNA), and saline. Thus, it is suggested that the nanomicelle effectively introduced IGF-1 into the muscle to induce muscle hypertrophy

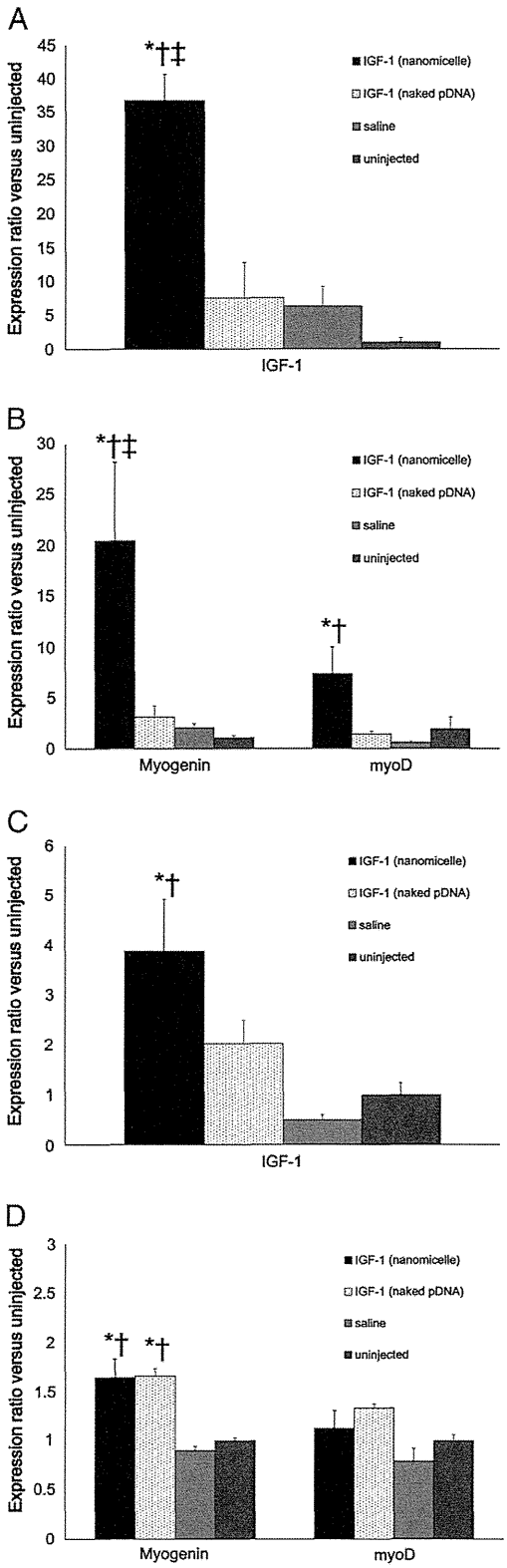

Fig. 1. Gene expression in skeletal muscle of quadriceps femoris (A, B) and triceps surae (C, D) after hydrodynamic injection, evaluated by real-time polymerase chain reaction (PCR) to determine mRNA expression levels of IGF-1 (A, C) and myogenic regulatory factors (myogenin and MyoD) (B, D). Data are presented as relative values to the uninjected control, as means ± standard error of the mean (SEM; n = 4 for quadriceps femoris and n = 5 for triceps surae), *$P < 0.05$ vs. saline; †$P < 0.05$ vs. uninjected control; ‡$P < 0.05$ vs. IGF-1 (naked pDNA).

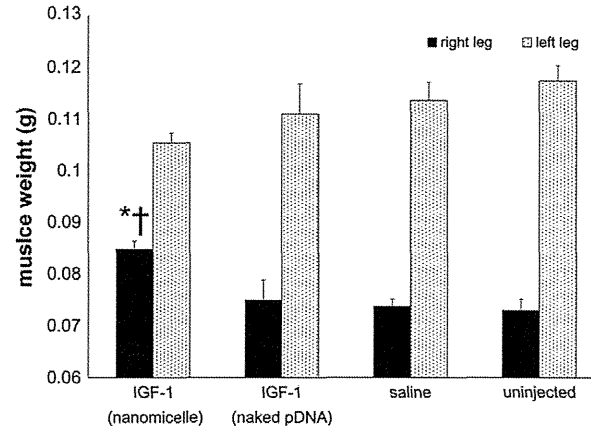

Fig. 2. Triceps surae muscle weight after right leg sciatic nerve injury, followed by the hydrodynamic injection of IGF-1-expressing pDNA or saline. Observed muscle weight values of right (injured) and left (normal) legs were presented. Data are expressed as means ± SEM (n = 5), *$P < 0.05$ vs. right leg of uninjected control mice; †$P < 0.05$ vs. right leg of saline.

through the upregulation of myogenic regulatory factors. The long-term effect of IGF-1 was also evaluated for triceps surae using nanomicelle. Although the muscle fiber area showed time-dependent decrease from Day 7 to Day 16 due to disuse atrophy, IGF-1-expressing pDNA introduced by nanomicelle showed a sustained effect to alleviate the atrophy to a significantly greater extent compared with saline control (Supplemental Fig. 1A–B). There were no apparent differences in the histopathology findings with regard to the muscle fibers (Fig. 3A and Supplemental Fig. 1A).

3.3. IGF-1-expressing pDNA promoted early recovery of motor function

To evaluate the effect on motor function, we evaluated walking track data. The sciatic functional index (SFI) was calculated from the footprints (see Materials and methods). Up to day 10 following sciatic nerve injury, all mice including those receiving IGF-1-expressing pDNA, negative control pDNA (expressing β-galactosidase), and untreated control mice showed almost no recovery of motor function (Fig. 4A). However, after that time, the group that received the hydrodynamic injection of IGF-1-expressing pDNA using polyplex nanomicelle showed significantly early recovery of motor function compared with other groups. The results are depicted in Figure 4B, where the numbers of mice showing full recovery represented by a SFI value > −15 are presented. By day 18, all mice that received the hydrodynamic injection of IGF-1-expressing pDNA using polyplex nanomicelle achieved full recovery, whereas in the other groups, not all mice reached full recovery even at day 25.

To compare the injection method of hydrodynamic injection with direct intramuscular (i.m.) injection, we performed the i.m. injection of IGF-1-expressing pDNA using nanomicelle or by the form of naked pDNA. As shown in Fig. 4C, the group of i.m. injection (nanomicelle and naked pDNA) showed similar profiles of motor function recovery as the control uninjected group, whereas the group receiving hydrodynamic injection showed significantly more rapid recovery. Thus, it is strongly suggested that the hydrodynamic injection is likely to be advantageous to achieve the therapeutic effect with the combined use of nanomicelle.

To further investigate the applicability of this treatment approach for more intractable conditions, we used a mouse model of diabetes mellitus. It is well known that peripheral nerve regeneration tends to be markedly impaired in association with diabetes mellitus, causing neuropathy with a poor prognosis [37,38]. Similar to that

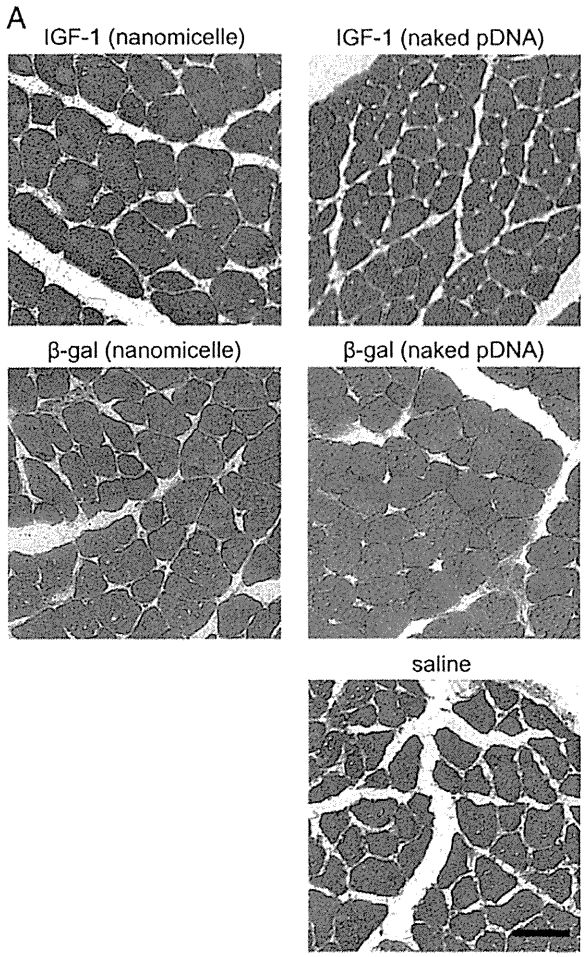

Fig. 3. Histologic analyses of muscle after hydrodynamic injection of IGF-1-expressing pDNA, β-galactosidase-expressing pDNA (using nanomicelle or by the form of naked pDNA) or saline. (A) Histology sections of quadriceps femoris on day 7 after sciatic nerve injury (scale bar, 50 μm). (B) Cross-sectional areas of individual muscle fibers in quadriceps femoris. More than 100 muscle fibers were subjected to statistical analyses. Error bars are SEM, $^{*}P < 0.05$ vs. saline; †$P < 0.05$ vs. β-gal (naked pDNA); #$P < 0.05$ vs. IGF (naked pDNA); ‡$P < 0.05$ vs. β-gal (nanomicelle).

described for normal mice, the sciatic nerve injury and concomitant hydrodynamic injection were applied to diabetic mice, and motor function was evaluated by walking track analysis. As shown in Fig. 5, the introduction of IGF-1-expressing pDNA using the polyplex nanomicelle promoted early recovery of SFI values compared with other groups similar to the results found with normal mice.

3.4. IGF-1 also promoted early recovery of sensation after sciatic nerve injury

Using the disease mouse model of diabetes mellitus, sensation in the distal area of sciatic nerve injury was evaluated after introduction of IGF-1-expressing pDNA. The paw pressure and acetone test were used to evaluate sensory changes (see Materials and methods). In the paw pressure test used to determine sensation to mechanical compression, the mice that received IGF-1-expressing pDNA using the polyplex nanomicelle showed remarkably shorter latencies to mechanical compression even on day 2 after sciatic nerve injury compared with other groups that received the naked form of IGF-1-expressing pDNA, negative control pDNA (expressing β-galactosidase), or untreated control mice (Fig. 6). In accordance with the results of motor function recovery, the control groups exhibited recovery to the normal level sensation around day 16.

The acetone test used to evaluate sensation to cold also revealed early recovery with introduction of IGF-1-expressing pDNA using polyplex nanomicelle, although the differences among the groups were not as prominent as that experienced with the paw pressure test (Fig. 7). The control groups showed recovery to the normal level by day 22.

4. Discussion

In this study, the efficacy of hydrodynamic introduction of IGF-1-expressing pDNA into skeletal muscle was demonstrated for the treatment of peripheral nerve injury. The expected role of IGF-1 is based on its myogenic functions to alleviate muscle atrophy gradually induced during a period of denervation. Although numerous approaches have been attempted to enhance nerve regeneration at the injury site, the inherently limited rate of axon elongation requires a prolonged period of treatment and leads to severe muscle atrophy and subsequent irreversible contracture of muscle and joint. The unique point of this study involves the direct targeting of the paralyzed muscle for treatment of peripheral nerve injury.

Compared with the routine method of intramuscular injection, which tends to induce severe tissue damage at the injected site, the hydrodynamic injection of polyplex nanomicelle into skeletal muscle is highly suitable to alleviate atrophy for the following reasons: 1) damage to the muscle is minimal and reversible and 2) this technique allows uniform distribution of gene introduction in the muscle fibers [22], which is apparently advantageous to obtain overall hypertrophy in the muscle fibers and consequent muscle-strengthening effects. With regard to safety, the hydrodynamic mechanism inevitably causes a temporary elevation of creatine phosphokinase (CPK) in the serum due to transient enhancement of the permeability of the plasma membrane; however, the CPK value returns to normal in a few days without causing any symptoms [21,22]. In addition, the nanomicelle was formed with the addition of anionic CS, which effectively reduced the inflammatory responses that may be induced by cationic polymers, leading to sustained transgene expression in the muscle [29]. Based on these features, the hydrodynamic injection of IGF-1-expressing pDNA using nanomicelle achieved the early recovery of motor function not only in wild-type mice (Fig. 4) but also in those with diabetes mellitus (Fig. 5).

Furthermore, the hydrodynamic injection is suitable for the treatment of peripheral nerve injury because this technique allows extensive pDNA introduction into muscles distal to the tourniquet. Paralysis occurs in all muscles distal to the nerve injury; thus, treatment should target all of these affected muscles. Although it is difficult to directly evaluate the individual functions of small muscles such as intrinsic muscles in the mouse foot, the effects on the small muscles were partially represented by SFI values, which contained the parameter of intrinsic muscle strength as represented by toe spread. It is reasonable to assume that the capability of efficient pDNA introduction into the distal small

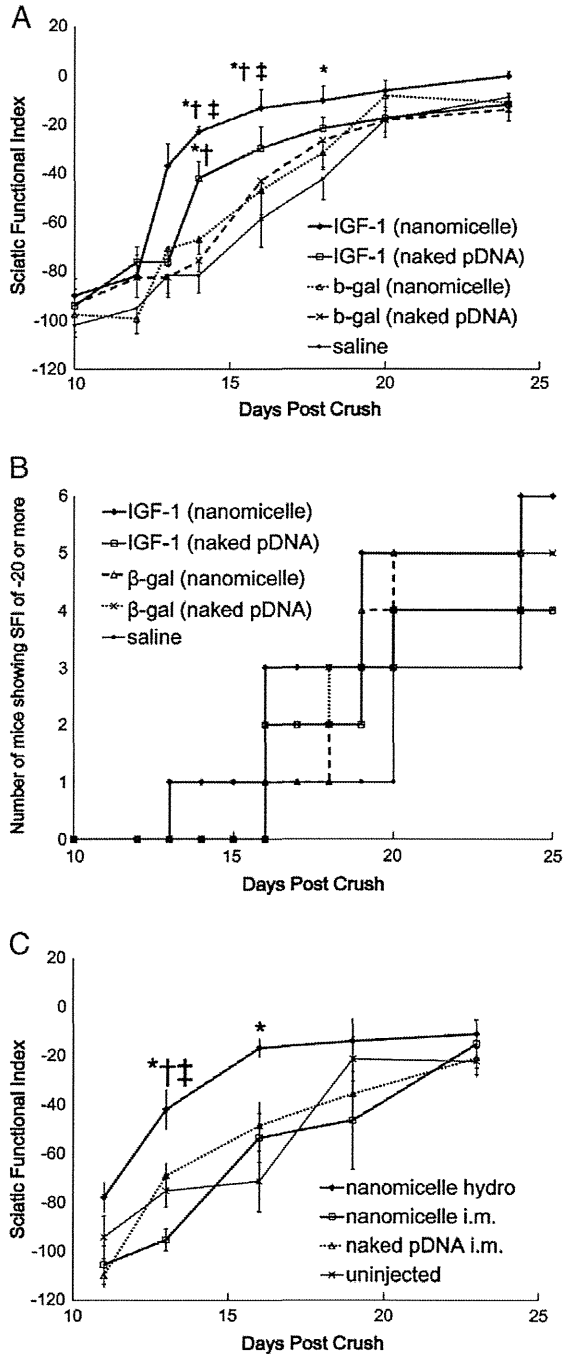

Fig. 4. Walking track analyses after sciatic nerve injury. (A) Sciatic functional index (SFI) calculated from footprints after hydrodynamic injection of IGF-1-expressing pDNA or β-galactosidase-expressing pDNA (using nanomicelle or by the form of naked pDNA). Data are expressed as means (n = 6). Error bars are SEM, *$P < 0.05$ vs. saline; †$P < 0.05$ vs. β-gal (naked pDNA); #$P < 0.05$ vs. IGF (naked pDNA); & $P < 0.05$ vs. β-gal (nanomicelle). (B) Numbers of mice showing recovery of motor function to SFI values >−15 in the experiment of (A). (C) Sciatic functional index (SFI) after intramuscular (i.m.) injection of IGF-1-expressing pDNA (using nanomicelle or by the form of naked pDNA) or hydrodynamic (hydro.) injection of nanomicelle. Data are expressed as means (n = 3). Error bars are SEM, *$P < 0.05$ vs. uninjected control; †$P < 0.05$ vs. i.m. of naked pDNA; ‡$P < 0.05$ vs. i.m. of nanomicelle.

muscles by hydrodynamic injection may contribute to the early recovery of motor functions after nerve injury.

It is interesting that, although the high transgene expression of IGF-1 was similarly obtained for quadriceps femoris and triceps surae after

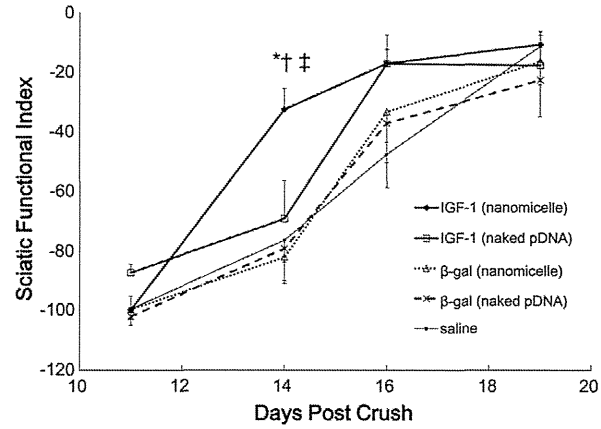

Fig. 5. Walking track analyses after sciatic nerve injury using diabetes mellitus disease model mice. Analyses were performed similar to those for wild-type mice (as presented in Fig. 4). Data are expressed as means (n = 5). *$P < 0.05$ vs. saline; †$P < 0.05$ vs. β-gal (naked pDNA); ‡$P < 0.05$ vs. β-gal (nanomicelle).

hydrodynamic injection of nanomicelle compared with that of naked pDNA, the effects on upregulating the myogenic regulatory factors (myogenin and myoD) were particularly more prominent in quadriceps femoris compared with triceps surae (Fig. 1B and D). A possible reason is that the femur lesion is more distant from the injection site (great saphenous vein), and the tissue damage and subsequent inflammatory responses are relatively lower than those in the lower leg, resulting in the clearer effects of IGF-1 introduction to induce muscle hypertrophy in quadriceps femoris.

Surprisingly, early recovery of sensation was also induced by the introduction of IGF-1-expressing pDNA. Although some papers reported that IGF-1 introduction promoted sensation recovery [39–41], the effects of IGF-1 on the sensory nerves were not as clear as those regarding the myogenic effect. It is probable that a significant amount of IGF-1 protein was secreted from the muscle, similar to that discussed in our previous paper, where the introduction of pDNA expressing a soluble form of vascular endothelial growth factor (VEGF) receptor-1 (sFlt-1) showed a remarkable effect on tumor growth regression by the secretion of sFlt-1 protein into the blood from the muscle [22]. Similar to sFlt-1, IGF-1 protein is likely to be secreted in the vicinity of the sciatic nerve injury site, promoting early recovery of sensation. Another possibility is that the muscle hypertrophy induced by IGF-1 caused an afferent effect on sensory nerves. Such effects are reported in physical

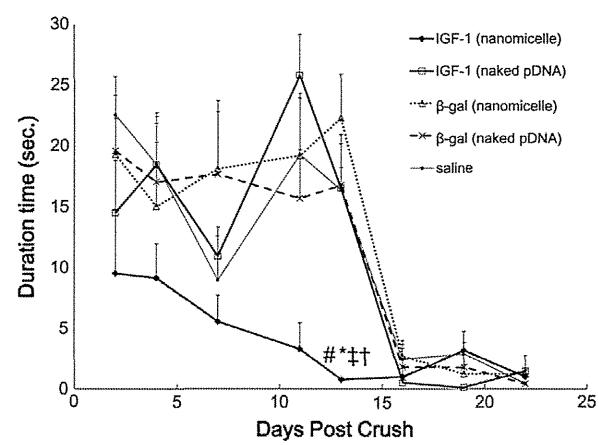

Fig. 6. Analyses of pain sensation in the paw after sciatic nerve injury. Data are expressed as means (n = 5). Error bars are SEM, *$P < 0.05$ vs. saline; †$P < 0.05$ vs. β-gal (naked pDNA); #$P < 0.05$ vs. IGF (naked pDNA); ‡$P < 0.05$ vs. β-gal (nanomicelle).

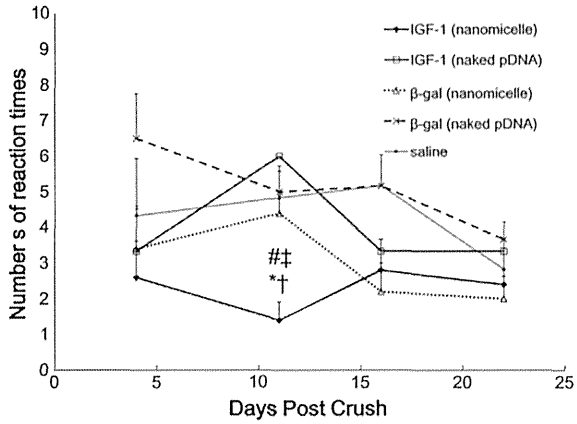

Fig. 7. Analyses of cold sensation after sciatic nerve injury. Data are expressed as means (n = 5). Error bars are SEM, $^{*}P < 0.05$ vs. saline; $\dagger P < 0.05$ vs. β-gal (naked pDNA); $\#P < 0.05$ vs. IGF (naked pDNA); $\ddagger P < 0.05$ vs. β-gal (nanomicelle).

training. For example, treadmill training stimulates the distal portion of the injured nerve and promotes nerve regeneration through activation of Schwann cell proliferation [42]. The detailed mechanism involved in rapid sensation recovery remains an unsolved issue; however, it is clear that rapid sensation recovery exerts a synergistic effect with muscle hypertrophy to produce a more favorable prognosis.

In conclusion, the introduction of IGF-1-expressing pDNA into skeletal muscle provided a remarkable therapeutic effect, promoting the recovery of motor function in a mouse model of sciatic nerve injury. The hydrodynamic injection of polyplex nanomicelle containing IGF-1-expressing pDNA maximized the effect of IGF-1 without causing any apparent tissue damage. This treatment achieved remarkable effects by alleviating disused muscle atrophy and promoting early recovery of motor function. We consider this approach to have potential to be used as the treatment for peripheral nerve injury.

Supplementary data to this article can be found online at http://dx.doi.org/10.1016/j.jconrel.2014.03.021.

Acknowledgments

We thank Dr. Toru Ogata (National Rehabilitation Center for the Persons with Disabilities, Saitama, Japan) for supplying technical information to make a mouse model of sciatic nerve injury. This work was financially supported in part by Grants-in-Aid for Scientific Research from the Japanese Ministry of Education, Culture, Sports, Science and Technology, Japan (MEXT) (K. I.), the Core Research Program for Evolutional Science and Technology (CREST) from the Japan Science and Technology Corporation (JST) (K. K.), and JSPS Core-to-Core Program, A. Advanced Research Networks (K.K. and K.I.). We thank Ms. Katsue Morii and Ms. Yoko Hasegawa (The University of Tokyo) for technical assistance.

References

[1] V.T. Ribeiro-Resende, A. Carrier-Ruiz, R.L. RM, R.A. Reis, R. Mendez-Otero, Bone marrow-derived fibroblast growth factor-2 induces glial cell proliferation in the regenerating peripheral nervous system, Mol. Neurodegener. 7 (2012) 34.
[2] S. Barati, P.R. Hurtado, S.H. Zhang, R. Tinsley, I.A. Ferguson, R.A. Rush, GDNF gene delivery via the p75(NTR) receptor rescues injured motor neurons, Exp. Neurol. 202 (2006) 179–188.
[3] F.C. Cheng, M.H. Tai, M.L. Sheu, C.J. Chen, D.Y. Yang, H.L. Su, S.P. Ho, S.Z. Lai, H.C. Pan, Enhancement of regeneration with glia cell line-derived neurotrophic factor-transduced human amniotic fluid mesenchymal stem cells after sciatic nerve crush injury, J. Neurosurg. 112 (2010) 868–879.
[4] V.J. Tom, H.R. Sandrow-Feinberg, K. Miller, C. Domitrovich, J. Bouyer, V. Zhukareva, M.C. Klaw, M.A. Lemay, J.D. Houle, Exogenous BDNF enhances the integration of chronically injured axons that regenerate through a peripheral nerve grafted into a chondroitinase-treated spinal cord injury site, Exp. Neurol. 239C (2012) 91–100.
[5] A. Brockington, C. Lewis, S. Wharton, P.J. Shaw, Vascular endothelial growth factor and the nervous system, Neuropathol. Appl. Neurobiol. 30 (2004) 427–446.
[6] F.R. Pereira Lopes, B.C. Lisboa, F. Frattini, F.M. Almeida, M.A. Tomaz, P.K. Matsumoto, F. Langone, S. Lora, P.A. Melo, R. Borojevic, S.W. Han, A.M. Martinez, Enhancement of sciatic nerve regeneration after vascular endothelial growth factor (VEGF) gene therapy, Neuropathol. Appl. Neurobiol. 37 (2011) 600–612.
[7] J.R. Florini, D.Z. Ewton, S.A. Coolican, Growth hormone and the insulin-like growth factor system in myogenesis, Endocr. Rev. 17 (1996) 481–517.
[8] A. Musaro, K. McCullagh, A. Paul, L. Houghton, G. Dobrowolny, M. Molinaro, E.R. Barton, H.L. Sweeney, N. Rosenthal, Localized Igf-1 transgene expression sustains hypertrophy and regeneration in senescent skeletal muscle, Nat. Genet. 27 (2001) 195–200.
[9] E.D. Rabinovsky, E. Gelir, S. Gelir, H. Lui, M. Kattash, F.J. DeMayo, S.M. Shenaq, R.J. Schwartz, Targeted expression of IGF-1 transgene to skeletal muscle accelerates muscle and motor neuron regeneration, FASEB J. 17 (2003) 53–55.
[10] T. Shavlakadze, J.D. White, M. Davies, J.F. Hoh, M.D. Grounds, Insulin-like growth factor I slows the rate of denervation induced skeletal muscle atrophy, Neuromuscul. Disord. 15 (2005) 139–146.
[11] G.R. Adams, S.A. McCue, Localized infusion of IGF-I results in skeletal muscle hypertrophy in rats, J. Appl. Physiol. 84 (1998) 1716–1722.
[12] C. Kasemkijwattana, J. Menetrey, P. Bosch, G. Somogyi, M.S. Moreland, F.H. Fu, B. Buranapanitkit, S.S. Watkins, J. Huard, Use of growth factors to improve muscle healing after strain injury, Clin. Orthop. Relat. Res. (2000) 272–285.
[13] A.M. Payne, Z. Zheng, M.L. Messi, C.E. Milligan, E. Gonzalez, O. Delbono, Motor neurone targeting of IGF-1 prevents specific force decline in ageing mouse muscle, J. Physiol. 570 (2006) 283–294.
[14] J.D. Schertzer, G.S. Lynch, Comparative evaluation of IGF-I gene transfer and IGF-I protein administration for enhancing skeletal muscle regeneration after injury, Gene Ther. 13 (2006) 1657–1664.
[15] E.R. Barton-Davis, D.I. Shoturma, A. Musaro, N. Rosenthal, H.L. Sweeney, Viral mediated expression of insulin-like growth factor I blocks the aging-related loss of skeletal muscle function, Proc. Natl. Acad. Sci. U. S. A. 95 (1998) 15603–15607.
[16] T. Takahashi, K. Ishida, K. Itoh, Y. Konishi, K.I. Yagyu, A. Tominaga, J.I. Miyazaki, H. Yamamoto, IGF-I gene transfer by electroporation promotes regeneration in a muscle injury model, Gene Ther. 10 (2003) 612–620.
[17] M.B. Alzghoul, D. Gerrard, B.A. Watkins, K. Hannon, Ectopic expression of IGF-I and Shh by skeletal muscle inhibits disuse-mediated skeletal muscle atrophy and bone osteopenia *in vivo*, FASEB J. 18 (2004) 221–223.
[18] S. Lee, E.R. Barton, H.L. Sweeney, R.P. Farrar, Viral expression of insulin-like growth factor-I enhances muscle hypertrophy in resistance-trained rats, J. Appl. Physiol. 96 (2004) 1097–1104.
[19] J.E. Stevens-Lapsley, F. Ye, M. Liu, S.E. Borst, C. Conover, K.E. Yarasheski, G.A. Walter, H.L. Sweeney, K. Vandenborne, Impact of viral-mediated IGF-I gene transfer on skeletal muscle following cast immobilization, Am. J. Physiol. Endocrinol. Metab. 299 (2010) E730–E740.
[20] F. Liu, Y. Song, D. Liu, Hydrodynamics-based transfection in animals by systemic administration of plasmid DNA, Gene Ther. 6 (1999) 1258–1266.
[21] J.E. Hagstrom, J. Hegge, G. Zhang, M. Noble, V. Budker, D.L. Lewis, H. Herweijer, J.A. Wolff, A facile nonviral method for delivering genes and siRNAs to skeletal muscle of mammalian limbs, Mol. Ther. 10 (2004) 386–398.
[22] K. Itaka, K. Osada, K. Morii, P. Kim, S.H. Yun, K. Kataoka, Polyplex nanomicelle promotes hydrodynamic gene introduction to skeletal muscle, J. Control. Release 143 (2010) 112–119.
[23] K. Itaka, K. Kataoka, Progress and prospects of polyplex nanomicelles for plasmid DNA delivery, Curr. Gene Ther. 11 (2011) 457–465.
[24] K. Itaka, K. Kataoka, Recent development of nonviral gene delivery systems with virus-like structures and mechanisms, Eur. J. Pharm. Biopharm. 71 (2009) 475–483.
[25] N. Kanayama, S. Fukushima, N. Nishiyama, K. Itaka, W.D. Jang, K. Miyata, Y. Yamasaki, U.I. Chung, K. Kataoka, A PEG-based biocompatible block catiomer with high buffering capacity for the construction of polyplex micelles showing efficient gene transfer toward primary cells, ChemMedChem 1 (2006) 439–444.
[26] K. Itaka, T. Ishii, Y. Hasegawa, K. Kataoka, Biodegradable polyamino acid-based polycations as safe and effective gene carrier minimizing cumulative toxicity, Biomaterials 31 (2010) 3707–3714.
[27] K. Itaka, S. Ohba, K. Miyata, H. Kawaguchi, K. Nakamura, T. Takato, U.I. Chung, K. Kataoka, Bone regeneration by regulated *in vivo* gene transfer using biocompatible polyplex nanomicelles, Mol. Ther. 15 (2007) 1655–1662.
[28] M. Harada-Shiba, I. Takamisawa, K. Miyata, T. Ishii, N. Nishiyama, K. Itaka, K. Kangawa, F. Yoshihara, Y. Asada, K. Hatakeyama, N. Nagaya, K. Kataoka, Intratracheal gene transfer of adrenomedullin using polyplex nanomicelles attenuates monocrotaline-induced pulmonary hypertension in rats, Mol. Ther. 17 (2009) 1180–1186.
[29] S. Uchida, K. Itaka, Q. Chen, K. Osada, K. Miyata, T. Ishii, M. Harada-Shiba, K. Kataoka, Combination of chondroitin sulfate and polyplex micelles from poly(ethylene glycol)-poly{N′-[N-(2-aminoethyl)-2-aminoethyl]aspartamide} block copolymer for prolonged *in vivo* gene transfection with reduced toxicity, J. Control. Release 155 (2011) 296–302.
[30] J.R. Bain, S.E. Mackinnon, D.A. Hunter, Functional evaluation of complete sciatic, peroneal, and posterior tibial nerve lesions in the rat, Plast. Reconstr. Surg. 83 (1989) 129–138.
[31] T. Kawamoto, M. Shimizu, A method for preparing 2- to 50-micron-thick fresh-frozen sections of large samples and undecalcified hard tissues, Histochem. Cell Biol. 113 (2000) 331–339.

[32] T. Kawamoto, Use of a new adhesive film for the preparation of multi-purpose fresh-frozen sections from hard tissues, whole-animals, insects and plants, Arch. Histol. Cytol. 66 (2003) 123–143.
[33] M.M. Inserra, D.A. Bloch, D.J. Terris, Functional indices for sciatic, peroneal, and posterior tibial nerve lesions in the mouse, Microsurgery 18 (1998) 119–124.
[34] T. Murakami, M. Arai, Y. Sunada, A. Nakamura, VEGF 164 gene transfer by electroporation improves diabetic sensory neuropathy in mice, J. Gene Med. 8 (2006) 773–781.
[35] M. Nakamura-Craig, R.L. Follenfant, Effect of lamotrigine in the acute and chronic hyperalgesia induced by PGE2 and in the chronic hyperalgesia in rats with streptozotocin-induced diabetes, Pain 63 (1995) 33–37.
[36] Y. Choi, Y.W. Yoon, H.S. Na, S.H. Kim, J.M. Chung, Behavioral signs of ongoing pain and cold allodynia in a rat model of neuropathic pain, Pain 59 (1994) 369–376.
[37] P. Muangman, L.A. Muffley, J.P. Anthony, M.L. Spenny, R.A. Underwood, J.E. Olerud, N.S. Gibran, Nerve growth factor accelerates wound healing in diabetic mice, Wound Repair Regen. 12 (2004) 44–52.
[38] J.M. Kennedy, D.W. Zochodne, Impaired peripheral nerve regeneration in diabetes mellitus, J. Peripher. Nerv. Syst. 10 (2005) 144–157.
[39] K.A. Sullivan, B. Kim, E.L. Feldman, Insulin-like growth factors in the peripheral nervous system, Endocrinology 149 (2008) 5963–5971.
[40] Q. Chu, R. Moreland, N.S. Yew, J. Foley, R. Ziegler, R.K. Scheule, Systemic insulin-like growth factor-1 reverses hypoalgesia and improves mobility in a mouse model of diabetic peripheral neuropathy, Mol. Ther. 16 (2008) 1400–1408.
[41] M. Miura, M. Sasaki, K. Mizukoshi, M. Shibasaki, Y. Izumi, G. Shimosato, F. Amaya, Peripheral sensitization caused by insulin-like growth factor 1 contributes to pain hypersensitivity after tissue injury, Pain 152 (2011) 888–895.
[42] T.B. Seo, M.J. Oh, B.G. You, K.B. Kwon, I.A. Chang, J.H. Yoon, C.Y. Lee, U. Namgung, ERK1/2-mediated Schwann cell proliferation in the regenerating sciatic nerve by treadmill training, J. Neurotrauma 26 (2009) 1733–1744.